RESEARCH ARTICLE

Initiation of dilute and concentrated pyroclastic currents from collapsing mixtures and origin of their proximal deposits

Greg A. Valentine[1]

Abstract

Numerical solution of the time-dependent conservation equations for mass, momentum, specific internal energy, and granular temperature in flows involving gas-particle mixtures is used to explore the initiation of pyroclastic currents from collapsing mixtures such as during fountaining eruptions. One objective is to determine when a depth-averaged granular flow model or a box model for dilute currents is most applicable for hazards modeling of pyroclastic currents produced by column collapse; a second objective is to gain insight into the formation of proximal breccia facies of ignimbrites. Collapsing gas-particle mixtures impacting a flat surface are modeled with mixtures of coarse particles that are poorly coupled with the gas phase and well-coupled fine particles. Resulting lateral flows are sensitive to the impact speed, overall particle concentration, and proportions of fine and coarse particles. For total particle concentrations of around 1 vol.%, an impacting mixture consisting of at least ~ 50% coarse particles, relative to fines, will tend to form a concentrated lateral underflow, which can be approximated by a depth-averaged granular flow model for hazard assessment purposes starting from the impact zone. Low total particle concentrations (e.g., total concentrations of ~ 0.1 vol.%) tend to produce dilute lateral flows that could be simplified to box model approaches for dilute pyroclastic currents. Larger total particle concentrations in impacting mixtures (~ 10 vol.%) produce granular underflows if they have any coarse particles, but these can be complicated by Mach number effects. For intermediate concentrations of the impacting mixture, a rough threshold for development of a concentrated underflow versus a dilute-only current is based upon the flux per unit area of coarse particles to the impact and their Stokes numbers. In general, some knowledge of the eruption column (fountain) conditions is required in order to make an informed decision as to which hazards modeling approach is most applicable for a given scenario. Modeling indicates that proximal breccias are related to influxes of coarse wall-rock material into an eruptive mixture, which increase both the total particle concentration and the proportion of coarse, dense clasts in the mixture that subsequently collapses and impacts the ground. The breccias record concentration of dominantly coarse clasts immediately upon impact and formation of concentrated flows that propagate laterally while expelled fines and gas flow rapidly overhead as dilute currents. Lateral and vertical heterogeneity in proximal deposits likely record rapid time and space variations in avalanches of material into eruptive vents, and the occurrence of breccia hummocks might record the temporary positions of impact zones.

Keywords Pyroclastic current · Pyroclastic density current · Pyroclastic flow · Multiphase flow · Ignimbrite

✉ Greg A. Valentine
gav4@buffalo.edu

[1] Department of Geology and Center for Geohazards Studies, University at Buffalo, Buffalo, NY 14260, USA

Introduction

Research on pyroclastic currents combines field-based studies of their deposits, experimental approaches, and theoretical modeling, which is the focus of this paper. Deposits of pumice-bearing pyroclastic currents (ignimbrites) produced by fountaining of an eruptive gas-particle mixture (a.k.a. column collapse) have been the subjects of numerous field studies. The deposits range in volume from fractions of a cubic kilometer to a few thousand cubic kilometers. Many

ignimbrites are very poorly sorted, massive, and strongly ponded in topographic lows (for example the main part of the Valley of Ten Thousand Smokes ignimbrite; Fierstein and Wilson 2005). Others have more complex facies that range from stratified and cross-stratified to massive and, while thickest in topographic lows, also drape over highs (for example, the Taupo ignimbrite; Wilson 1985). Facies and fabric analyses (including anisotropy of magnetic susceptibility; Baer et al. 1997; Ort et al. 2003; Cas et al. 2011) have led to interpretations that the parent pyroclastic currents range from concentrated granular dispersions with elevated pore pressures that promote mobility to more dilute currents where clast transport is dominated by turbulent suspension and depositional processes are modified by parameters such as suspended-load sedimentation rates (Branney and Kokelaar 2002; Sulpizio et al. 2014). Most ignimbrites contain dense lithic clasts as a minor component in terms of volume fraction (less than ~ 10%) throughout much of their dispersal (Valentine et al. 2019), but proximal facies can have abundant lithic-rich breccia and tuff breccia horizons (e.g., Druitt and Sparks 1982; Druitt and Bacon 1986; Suzuki-Kamata and Kamata 1990; Bear et al. 2009). The formation of such proximal facies has been related in various ways to the transition from a falling gas-particle mixture (from column collapse/fountaining) to a laterally flowing current (Wright and Walker 1977; Druitt and Sparks 1982; Walker 1985). This transition, referred to here as the impact zone, is important to understand because the characteristics of an outgoing pyroclastic current are strongly influenced by the behavior of various clast types there.

Experimental research on pyroclastic currents is quite varied, ranging from analog experiments to laboratory- and large-scale multiphase studies (Roche and Carazzo 2019); these scaled experiments generally focus on very specific aspects of flow dynamics. Laboratory-scale work includes studies related to internal processes such as particle-particle and flow-substrate interaction (Dufek and Manga 2008; Dufek et al. 2009; Roche et al. 2013, 2016; Fauria et al. 2016); heat transfer between particles and surrounding gas (Moitra et al. 2018); turbulent suspension of particles (Weit et al. 2018, 2019); and the role of turbulence, granular interactions, and pore pressure on concentrated flows (e.g., Andrews and Manga 2011, 2012; Roche et al. 2008, 2011; Roche 2012; Andrews 2014; Chédeville and Roche 2018). Large-scale experiments are of growing importance, seeking to capture as much as possible of the physics of natural currents generated by collapsing gas-pyroclast mixtures (Dellino et al. 2007, 2014, 2019; Lube et al. 2015; Breard et al. 2016; Breard and Lube 2017). These large-scale experiments include a collapsing/impacting component as gas-particle mixtures fall from a fountain height or a hopper, but these necessarily do not involve the full range of impact speeds (10 s m/s to more

than 100 m/s) and particle concentrations (as low 10^{-2}–10^{-3}) that might be expected in an eruption.

Numerical fluid-dynamic models are critical tools in both advancing our understanding of pyroclastic currents and for predicting volcanic hazards. Multiphase models solve two- and three-dimensional, time-dependent conservation equations for mass, momentum, and energy of gas-particle fields, treating gases and different particle sizes/densities as interpenetrating continua (e.g., Dartevelle 2004; Dufek and Bergantz 2007a, b; Esposti Ongaro et al. 2008, 2012). Such models require substantial development, setup, and computation time and, while extremely useful for basic research on pyroclastic currents and for detailed evaluation of specific eruption scenarios, they are not practical for hazards assessments that involve analysis of a wide range of possible conditions and that often need relatively faster turnaround in order to support decision-making and communications with stakeholders. Instead, models used routinely in volcanic hazards assessments are designed around end-member behaviors of pyroclastic currents. Concentrated currents that behave as granular dispersions are simulated with depth-averaged (also referred to as shallow-water approximation) approaches that do not model vertical variations in flow parameters, but can account for flow over complex topography (Patra et al. 2005; Kelfoun et al. 2009). On the other end of the spectrum, box models are used for dilute currents, where particle transport is dominated by turbulent suspension; they account for spreading of a gravity current with density evolving due to sedimentation of particles (Dade and Huppert 1996; Esposti Ongaro et al. 2016). A range of theoretical approaches have also been developed that add complexity to the depth-averaged granular and box model turbulent approaches and/or that simplify some aspects of the full multiphase approach (e.g., Bursik and Woods 1996; Shimizu et al. 2019; Doronzo et al. 2010; Doyle et al. 2008; Kelfoun 2017), but the depth-averaged and box model methods are the most commonly used for hazards assessments. These assume either a concentrated (granular) or dilute (fully turbulent) condition, respectively, in the pyroclastic currents of interest. Their initial conditions are typically described as a pile of granular matter or a specified flow depth (head) in the source area for the depth-averaged case, which is an approximation for a lava dome collapse or slope failure, or as a "dam break" release of gas-particle mixture in the box model case. Some workers have extended these tools to fountaining scenarios (e.g., Tierz et al. 2018; Neri et al. 2015) but there are questions about how well the dynamics of a falling and turning multiphase mixture are captured with these initial conditions, particularly in cases of sustained flux.

Early multiphase modeling indicated that coarse and/or dense clasts in a collapsing mixture concentrate rapidly in the impact zone (Valentine and Wohletz 1989; Dartevelle et al. 2004), but the implications were not explored until recently. Sweeney and Valentine (2017) began a study aimed at

understanding impact zone dynamics using the multiphase approach. They developed a dimensionless parameter called the impact Stokes number (St_{imp}), which, like Stokes numbers in general, is a ratio of a measure of the time (t_p) over which a particle can respond to changes in its carrier fluid velocity, relative to the time scale (t_f) of the fluid changes (Burgisser and Bergantz 2002; Dufek 2015). The particle time-scale measure, t_p, is a function of particle density and size (ρ_p and d_p, respectively), and the density and viscosity (ρ_g, μ_g) of the surrounding gas or dusty-gas, i.e. $t_p = \frac{(\rho_p - \rho_g)d_p^2}{18\mu_g}$. St_{imp} specifically describes the ability of a particle to respond to the changes in flow speed and direction that are associated with impact, such that $t_f = \delta/v_{imp}$, with δ being the length scale over which vertical speed of the collapsing mixture decelerates to zero at impact and v_{imp} being the falling speed of the mixture prior to deceleration. Valentine and Sweeney (2018) qualitatively discussed how the proportion of high vs low St_{imp} particles (poorly coupled to the gas) in the impacting mixture influences the properties of the outgoing lateral flow (pyroclastic current). They also showed that compressible flow effects can strongly influence the proximal development of pyroclastic currents as they move away from impact. This paper concludes our study of the impacting gas-particle mixtures with a quantitative emphasis on the basal particle concentrations of outgoing currents. Although the numerical modeling is simplified compared with natural cases, the results provide insight into conditions under which a depth-averaged granular flow model versus a box model for dilute flows can be best used for hazards modeling of pyroclastic currents produced by fountaining and provide further insight into the development of proximal ignimbrite facies.

Approach and terms

Governing equations

The model equations represent conservation of mass, momentum, and specific internal energy for gas and for fields of particles of multiple size/density classes, implemented in the numerical model MFIX (Syamlal and Pannala 2011; Benyahia et al. 2012; Syamlal et al. 2017). Gas and particle fields are all modeled within a stationary (Eulerian) reference frame. Each phase (gas and particle class, represented by subscripts g and m, where $m = 1$ through M particle classes) is modeled as occupying the same volume in proportion to its respective volume fractions (ϵ). Using index notation for the Cartesian coordinates (i, j, k), the governing equations are:

$$\frac{\partial}{\partial t}\left(\epsilon_g \rho_g\right) + \frac{\partial}{\partial x_j}\left(\epsilon_g \rho_g U_{gj}\right) = 0 \qquad \text{(gas),} \qquad (1)$$

$$\frac{\partial}{\partial t}\left(\epsilon_m \rho_m\right) + \frac{\partial}{\partial x_j}\left(\epsilon_m \rho_m U_{mj}\right) = 0 \qquad \text{(particles),} \qquad (2)$$

$$\frac{\partial}{\partial t}\left(\epsilon_g \rho_g U_{gi}\right) + \frac{\partial}{\partial x_j}\left(\epsilon_g \rho_g U_{gj} U_{gi}\right)$$
$$= -\epsilon_g \frac{\partial P_g}{\partial x_i} + \frac{\partial \tau_{gij}}{\partial x_j} - \sum_{m=1}^{M} I_{gmi} + \epsilon_g \rho_g g_i \qquad \text{(gas),} \qquad (3)$$

$$\frac{\partial}{\partial t}\left(\epsilon_m \rho_m U_{mi}\right) + \frac{\partial}{\partial x_j}\left(\epsilon_m \rho_m U_{mj} U_{mi}\right) = -\epsilon_m \frac{\partial P_g}{\partial x_i} + \frac{\partial \tau_{mij}}{\partial x_j} \qquad (4)$$
$$+ I_{gmi} - \sum_{l=1}^{M} I_{mli} + \epsilon_m \rho_m g_i \qquad \text{(particles),}$$

$$\epsilon_g \rho_g C_{pg}\left[\frac{\partial T_g}{\partial t} + U_{gj}\frac{\partial T_g}{\partial x_j}\right] = -\frac{\partial q_{gj}}{\partial x_j} + \sum_{m=1}^{M} \gamma_{gm}\left(T_m - T_g\right)$$
$$+ \gamma_{Rg}\left(T_{Rg}^4 - T_g^4\right) \qquad \text{(gas), (5)}$$

and

$$\epsilon_m \rho_m C_{pm}\left[\frac{\partial T_m}{\partial t} + U_{mj}\frac{\partial T_m}{\partial x_j}\right] = -\frac{\partial q_{mj}}{\partial x_j} - \gamma_{gm}\left(T_m - T_g\right) \qquad (6)$$
$$+ \gamma_{Rm}\left(T_{Rm}^4 - T_m^4\right) \qquad \text{(particles).}$$

Equations 1 and 2 are conservation of mass for gas and particle fields, Eqs. 3 and 4 are conservation of momentum, and Eqs. 5 and 6 are conservation of specific internal energy (see Table 1 in the Appendix for notation). This set of equations is similar to other multiphase modeling studies of explosive volcanic eruptions, to which a reader can refer for explanation of the terms (e.g., Neri and Dobran 1994; Neri et al. 2003; Dartevelle 2004; Esposti Ongaro et al. 2012; Sweeney and Valentine 2017; Valentine and Sweeney 2018).

Equations 1–6 are closed by equations of state for the gas and particle phases and by constitutive models that describe rheology of the phases and interactions between them in the form of drag (*I*-terms in Eqs. 3 and 4) and heat transfer (γ-terms in Eqs. 5 and 6). The constitutive relationships used for gas-particle drag are highlighted here because of their importance to the study; they vary depending upon local particle volume concentrations, such that when total particle concentration $\epsilon_{tot} > 0.2$, a relationship derived from the Ergun model for gas flow through particle beds is used (Table 2 in the Appendix; Ergun 1952). At lower concentrations, the gas-particle momentum exchange is derived from drag on ensembles of individual particles. Different particle classes also exert drag on each other (particle-particle drag) through collisions and friction, which depend upon the size and local concentration of the particle classes through a radial distribution function (Table 2 in the Appendix), and are based upon a kinetic theory approach (Syamlal 1987). The calculations reported here all have gas and particles at a temperature of 20 °C, so

the interphase heat transfer functions are not laid out (see Benyahia et al. 2012).

The solid stress tensor τ_{mij} in Eq. 4 is expressed as

$$\tau_{mij} = \tau_{mij}^k + \quad \tau_{mij}^f \qquad , \qquad (7)$$

where the k and f superscripts refer to the kinetic and frictional components of stress. The kinetic stress term accounts for the random motion and inelastic collisions of particles. Frictional stresses occur at high particle concentrations ($\epsilon_{tot} > 0.5$ in this paper) where sliding contacts between particles become important. Modeling the solid stresses involves an additional conservation equation for Θ_m, the variance of the fluctuating component of particle velocities ($\Theta_m = \frac{1}{3}\langle u_{mi}^{'\,2} \rangle$, where $u_{mi}^{'}$ is the fluctuating velocity component of particle class m in the ith direction and the angle brackets indicate ensemble average). This parameter is often referred to as granular temperature due to its analogy to thermal energy in a gas. The conservation equation is (Benyahia et al. 2012):

$$\frac{2}{3}\rho_m \left[\frac{\partial \epsilon_m \Theta_m}{\partial t} + \frac{\partial \epsilon_m U_{mj} \Theta_m}{\partial x_j} \right]$$
$$= \frac{\partial}{\partial x_i}\left(\kappa_m \frac{\partial \Theta_m}{\partial x_i} \right) + \tau_{mij}^k \frac{\partial U_{mi}}{\partial x_j}$$
$$+ \Pi_m - \epsilon_m \rho_m J_m \qquad . \qquad (8)$$

Here, the first and second term on the left-hand side are the time rate of change and the advection of granular temperature, respectively. The first term on the right-hand side is conduction of granular temperature, the second is production through shear, the third is dissipation due to particle-fluid drag, and the final term is dissipation through inelastic collisions. Closure equations for the right-hand side terms (Table 3 in the Appendix) are derived from the kinetic theory approach of Srivastava and Sundaresan (2003), but modified to account for multiple particle fields (Benyahia et al. 2012). Equations 7 and 8 and their associated constitutive models (Table 3 in the Appendix) allow simulation of a full spectrum of gas-particle regimes within a single flow field as occurs in natural pyroclastic currents, from dilute conditions to concentrated flow where particle-particle interactions dominate momentum transport, and deposition (see Dartevelle 2004; Breard et al. 2019a).

Model and problem setup

MFIX is an open-source code (version 2016.1; access at mfix. netl.doe.gov) that solves the above conservation equations using a finite volume approach; it is widely used in industrial and energy applications, with growing application to volcanic gas-particle flows (e.g., Dartevelle 2004;

Dartevelle and Valentine 2007, 2008; Dufek and Berganz 2007a, b; Sweeney and Valentine 2015; Breard et al. 2019a, b). Valentine and Sweeney (2018) summarize verification and validation (confirmation) studies that demonstrate the model's ability to accurately represent gas-particle systems including shock-tube, overpressured jets, fluidized particle beds, and impinging jets. Breard et al. (2019a) documented how experimental dam-break concentrated flows (Roche et al. 2005, 2008, 2010) are simulated well by MFIX when the granular temperature transport equation is used with the Srivastava and Sundaresan (2003) model, as is done in this study.

The focus here is on the transition from falling to laterally flowing gas-particle mixtures as would be produced by fountaining eruptions (collapsing columns; Fig. 1a). Rather than simulating the entire fountain structure, the model domain is set up to capture the final stages of descent, followed by impact and lateral flow of the mixtures (Fig. 1b). This allows control of the impacting velocity and mixture properties and high grid resolution for the processes of interest. The domain is a half-space, such that the part of the mixture that would flow back towards the eruptive vent is not shown; that backflowing portion would experience the same processes as the outgoing flows emphasized below, albeit potentially complicated by interaction with the erupting jet. The simulations are two-dimensional which is considered appropriate for the flow-turning processes that are expected to dominate over three-dimensional turbulence effects in the immediate vicinity of the impact zone. For consistency, and due to the confidence associated with previous work on this topic, the Cartesian domain and mesh resolution ($\Delta x = \Delta y = 0.5$ m) are the same as in Sweeney and Valentine (2017) and Valentine and Sweeney (2018) (Table 4 in the Appendix).

Thirty-six simulations were conducted with varying combinations of total particle fraction, proportion of coarse and fine particles, and impact speed (Table 5 in the Appendix). Modeled impact speeds (50–100 m/s) correspond to free-fall from heights (fountain heights) of $\sim$ 125–500 m. The particle fractions of 10^{-2}–10^{-3} are reasonable for eruptive mixtures with $\sim$ 1–8 wt% H_2O vapor, neglecting any entrained air, introduction of lithic debris into the mixture, or particle concentrating effects in the parent fountain; concentrations less than $\sim 10^{-4}$ would not be significantly denser than dry ambient air ($\sim$ 1.3 kg/m³). The high end of the particle loading ($\epsilon_{tot} = 0.1$ to 0.01) would correspond to a low gas content eruptive mixture such as might occur when a large quantity of lithic debris is introduced to an eruptive jet(s) during caldera collapse, or to lava dome collapse-generated mixtures. To simplify the problem, there are no imposed temperature variations in the domain; both the ambient and the inflowing mixture are set at 20 °C. This also avoids overestimation of heat exchange between gas and the large particles, which are an essential component of the work here, due to their relatively high Biot number (see Moitra et al. 2018). Although volcanic flows are

Fig. 1 **a** Conceptual illustration of pyroclastic fountain and portion of the structure that is modeled in the computational domain. **b** Computational domain and boundary conditions
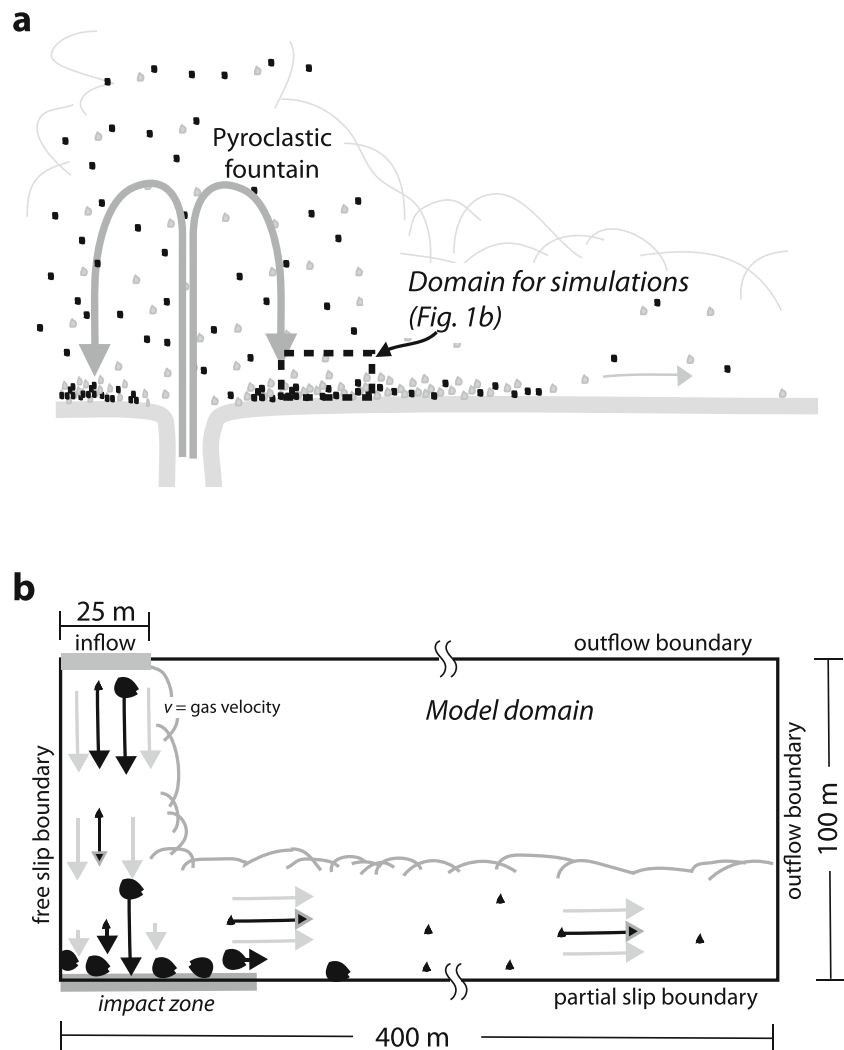
hot with cool ambient, the dynamics of interest are mainly related to gas-particle momentum coupling over time scales of seconds and are not affected by heat transfer (note that as a pyroclastic current travels away from impact, mixing with ambient air and thermal effects will become increasingly important). Table 4 in the Appendix provides initial and boundary conditions common to all simulations; note that the bottom boundary (ground) is a partial slip boundary for the particle phase. Impacting mixtures are monodisperse and bi-disperse (two particle classes with densities of 2000 kg/m^3 and diameters of 0.1 mm and 1 cm). Clearly this is a simplification compared with natural volcanic mixtures, but the two sizes capture sufficiently the range of particle-gas responses and coupling between fine and coarse particles to allow insights into flow conditions. Simulations are compared at $t = 6$ s after the inflow at the top of the domain begins, which, for most of the simulated flows (impact speeds of 50 m/s), was a sufficient time for the slowest currents to propagate laterally at least three times the width of the impact zone, but a short enough time that the fastest currents remained within the high-

resolution but spatially limited computational domain (note that for four of the 100 m/s runs, the domain height was 200 m instead of the normal 100 m, meaning that both height and the higher speed need to be accounted for in comparing the flow properties at $t = 6$ s with other runs; Table 5 in the Appendix).

Terms

For the remainder of the paper, the following terms will have specific, quantitative meaning when applied to the computational results. (1) *Coarse* particles have diameters of 1 cm while *fine* particles are 0.1 mm in discussion of the simulations. (2) *Impact zone* refers to the part of the bottom boundary (ground) directly under the falling (impinging) mixture. The width of this zone is approximately the same as the width of the impinging flow, ∼ 25 m in the simulations. (3) *Concentrated* flow is defined as having gas volume fraction $\epsilon_g \leq 0.8$ (equivalent to $\epsilon_{tot} > 0.2$, or 20 vol.%) where the Ergun model for gas-particle drag applies. With the material

properties used in this work, this criterion corresponds to a bulk particle density of 400 kg/m^3, where bulk particle density is $\sum_{m=1}^{M} (\epsilon_m \rho_m)$. At particle concentrations above $\sim$ 20 vol.% (up to close-packing), particle interactions play a major role in momentum transport within a flow in addition to having a different gas-particle drag behavior. Conversely, *dilute* flows or currents correspond to total particle concentrations below 20 vol.% in this paper. This criterion is internally consistent with the gas-particle momentum exchange model used here, but it is worth noting that experimental studies have shown that full support of dispersed particles in turbulent gas-particle flows requires total particle concentrations less than 2–5 vol.%; at higher concentrations, particles form narrow clusters or bands that settle at speeds faster than the settling speed of individual particles (Weit et al. 2018, 2019; see also Breard et al. 2016; Breard and Lube 2017). Although such clustering is not resolved in the modeling here, particle concentrations between $\sim$ 2 and 20 vol.% are expected to exhibit such clustering in natural flows, representing a transitional regime between fully dilute flow and concentrated flow where pore pressure may develop along with substantial particle-particle interaction. Finally, *underflow* is used to emphasize that the concentrated portions of the modeled flow fields are thin zones along the bottom boundary.

Results

Overall phenomenology and caveats

The impacting mixture flows into the computational domain, starting at $t = 0$, from the 25-m-wide inflow boundary (Fig. 1b) with specified vertical speed, pressure (equal to the ambient in all cases), and particle concentrations for the coarse and fine fractions (Table 5 in the Appendix). Gas and particle velocities are the same at the inlet, but may differ somewhat as the mixture approaches impact; this is most evident for simulations with abundant coarse particles which accelerate under gravity and are less affected by drag of the gas than fine particles (Sweeney and Valentine 2017). As the mixture nears the impact zone, displaced air, which entrains a small fraction of particles, jets outward along the ground. This small, but fast, jet is not of interest here since I focus on the main lateral flows during sustained impact, but its effects are seen in some plots of simulation data seen below.

Three main regimes are seen once the mixture turns and flows laterally away from the impact zone (Valentine and Sweeney 2018). (1) The outgoing flow will be dilute when the impacting mixture is subsonic and dominated by fine particles (low St_{imp}; Fig. 2a). (2) In subsonic cases with large proportions of coarse particles (high St_{imp}), the particles form a thin concentrated flow with a higher proportion of coarse relative to fine particles compared with the impacting mixture. This concentration-upon-impact process results in expulsion of interstitial gas, which forms a faster jet of gas that carries most (but not all) of the fines over the top and ahead of the granular underflow (Fig. 2b). (3) When impacting flow speed exceeds the mixture sound speed (Mach number greater than unity; Table 5 in the Appendix), the mixture compresses and decelerates through a bow shock above the impact zone and emerges as an overpressured, supersonic lateral flow that undergoes one or more expansion-recompression structures (Fig. 2c) until its pressure is balanced with ambient (Valentine and Sweeney 2018). In such cases, the proximal variations in particle volume fraction are dominated by expansion and compression of the gas phase. Note that high Mach number can be related to high flow speed and/or to high concentrations of fine particles that reduce the mixture sound speed.

The concentrated basal portion of the flow field (underflow) that formed in many of numerical simulations (e.g., Fig. 2b) was typically one to a few cells thick and thus poorly resolved (similar to Dartevelle et al. 2004). Breard et al. (2019a) showed that MFIX reasonably represents a concentrated flow front, compared with experimental results, even when the front thickness is as small as twice the cell size, when the solid stresses are modeled with the approach of Srivastava and Sundaresan (2003). Dartevelle et al.'s (2004) grid sensitivity study concluded that a mesh with up to 5-m-high cells along the bottom boundary adequately captured propagation and deposition of a concentrated underflow, when using MFIX for fountain-produced pyroclastic current simulations (compare with 0.5-m-high cells used here). It is possible that the numerical results presented here exaggerate the lateral flow distance of the granular underflow due to the mesh resolution, but grid sensitivity study indicated that halving the mesh size from 50 to 25 cm did not substantially change the basic result (Online Resource 1) while it did substantially increase the computing requirements. It is also important to maintain mesh sizes that are not so small relative to particle sizes that the continuum approximation is violated for the particle fields (for example, these mesh sizes imply $\sim 10^3$ and 10^2 particles per cell volume in three dimensions, for $\epsilon_c = 0.01$ and mesh sizes of 50 and 25 cm, respectively). Thus, I view the results here for concentrated flows as a reasonable proxy for reality at least in terms of *relative* variations. Nevertheless, the results are pushing the limits of the finite volume solution to Eqs. 1–6 and 8, effectively modeling the thin underflow as a depth-averaged flow. The problem of resolving very thin domains within a larger flow field points to a need to develop innovative numerical methods in order to more rigorously tackle this problem in two and three dimensions (see also Breard et al. 2019a).
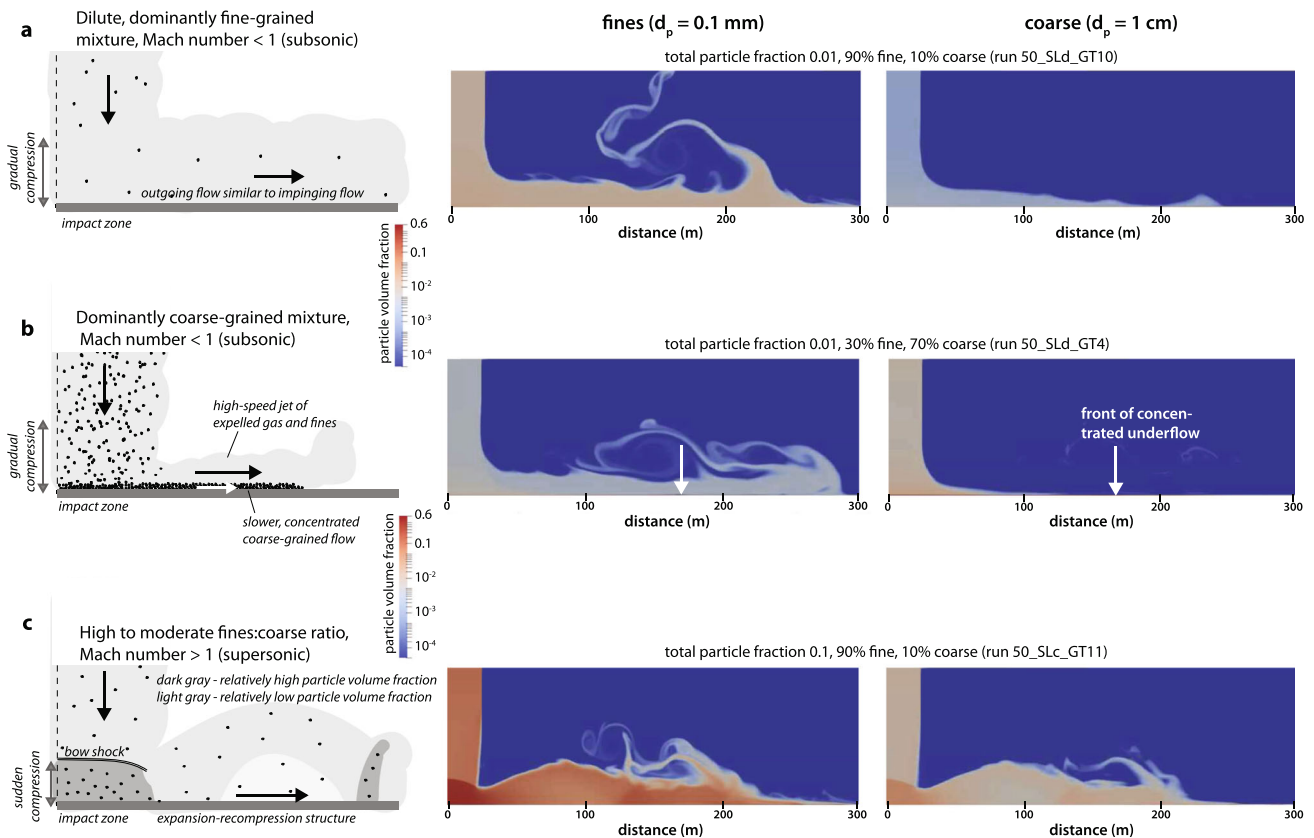
Fig. 2 Three different types of flow fields resulting from impact of collapsing gas-particle mixtures. Left panels show conceptual illustrations (modified from Valentine and Sweeney 2018), while middle and right panels show corresponding simulation results in terms of fine and coarse particle volume concentrations, respectively (note color scale). Simulation domains are 100 m high, impact speed is 50 m/s, and $t = 6$ s in all cases shown here. **a** Fines-dominated, subsonic impacting mixture. In simulation, the outgoing flow is dilute, with coarse particle concentration highest in the lower portion of the flow (but $\epsilon_c < 0.05$). **b** Coarse-dominated, subsonic impacting mixture. Large particles (high St_{imp}) concentrate upon impact forming a thin granular underflow while expelling gas and fines, which produce a faster-traveling, fine, and dilute flow forms above it. Front of the concentrated underflow indicated by arrow. **c** Fines-dominated but supersonic impacting mixture. Flow field is strongly affected by compressible flow effects of compression (at impact) and expansion-recompression (outgoing flow). Most of the variations in particle concentration are due to compression/expansion of the gas phase rather than gravity segregation in this proximal zone

Effects of proportions of coarse and fine particles

Series of simulations were completed for impact speeds of 50 and 100 m/s; total particle volumetric concentrations $\epsilon_{tot} = 0.1$, 0.01, and 0.001; and for varying proportions of coarse and fine particles (Table 5 in the Appendix). Most of the $\epsilon_{tot} = 0.1$ cases are strongly influenced by compressible flow effects due to the low sound speed caused by relatively high concentrations of fine particles. None of the modeled $\epsilon_{tot} = 0.001$ cases produced concentrated underflows within the simulated times of 6 s. Thus, to explore the effects of the proportions of coarse and fine particles, I focus on the $\epsilon_{tot} = 0.01$ cases (Figs. 3 and 4).

In order to understand the effects of varying proportions of particle sizes, it is useful to first understand the coarse- and fines-only end-member cases. In the coarse-only case, particles concentrated to near close-packing upon impact and a concentrated flow outside the impact zone, with $\epsilon_c \approx 0.25$

(bulk density ~ 500 kg/m^3; Fig. 3 upper left) and propagated outward at speeds up to ~ 20 m/s (Fig. 4). Expelled gas flowed rapidly (speeds up to ~ 90 m/s) over the top of the underflow and past it (this produces the peak in particle speed beyond the concentrated flow, even though ϵ_c is negligible, but not zero, there). At the other end of the spectrum, a fines-only case produced a dilute-only lateral flow with $\epsilon_f \approx 0.03$ (bulk density ~ 60 kg/m^3; Fig. 3). Cases where the impacting flow was dominantly coarse, with up to equal proportions of coarse and fine particles, produced concentrated outgoing flows propagated at speeds between 30 and 50 m/s, the speeds increasing with increasing fines fraction (Figs. 3 and 4). While concentrated flows (by the criteria used in this paper) were produced with up to 50% fines, ϵ_{tot} of the outgoing flow decreased with increasing fines.

Outgoing flows along the ground were depleted in fine particles relative to the impacting mixtures. For example, the 70% coarse, 30% fines case produced a lateral concentrated
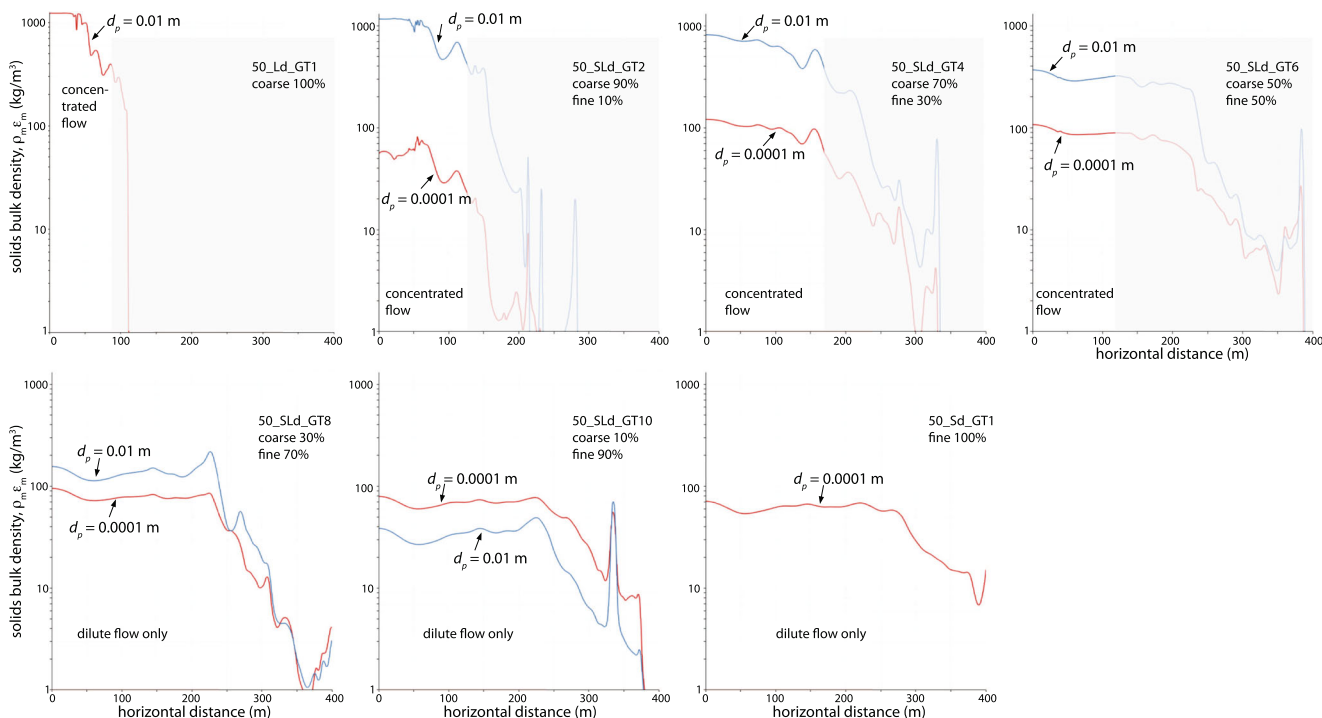
Fig. 3 Effect of proportions of coarse and fine particles in impacting flow on bulk particle density ($\rho_m\epsilon_m$) of the resulting lateral flows, measured at bottom of domain. Impact speed is 50 m/s, total particle concentration is 0.01, and $t = 6$ s in all cases. A total (coarse plus fines) bulk density of 400 kg/m³ or greater is taken to record concentrated flow. For reference, bulk densities of 10 and 1000 kg/m³ correspond to 0.5 and 50 vol.% particles, respectively. First plot (upper left) is a run with only coarse particles. Proportion of fines increases progressively to 100 vol.% in the final plot. Cases with up to 50 vol.% coarse particles form concentrated underflows (to the left of shaded areas in the first four plots) upon impact, while others form only dilute flows. Note that the "distal" parts of the plots record an initial jet caused by displacement of air (with a small fraction of entrained particles) upon initial impact of the collapsing mixture, which is not of interest to this study

flow with about 85% coarse and 15% fine particles, and the case with equal proportions of sizes had a lateral flow with ~ 75% coarse particles (Fig. 3). In these simulations, fines were preferentially sorted at the impact zone into the overriding dilute part of the flow field. This can be compared with Dellino et al.'s (2007) large-scale experiments of collapsing mixtures of natural pyroclastic material. For example, they report an example of a mixture with $\epsilon_{tot} \approx 0.014$ (bulk density of 22.8 kg/m³ and average particle density of 1630 kg/m³) that collapsed from a height of ~ 5 m. Deposits at the impact site had a very similar grain size distribution (slightly fines-depleted) to that of the initial mixture, indicating a lack of size sorting processes in the impact zone. The experimental mixture impacted the ground at a speed of 10.6 m/s (Dellino et al. 2007). The larger effect of impact sorting in the numerical results here might result from the larger impact speeds and/or the simpler particle size distribution.

The variations in outgoing lateral flows summarized above can be related in part to the impact Stokes numbers of coarse particles. With increasing proportion of fines, St_{imp} decreases from 735 to ~ 3 for coarse particles ($\epsilon_{tot} = 0.01$ cases) due to drag exerted by fine particles in addition to the gas as expressed in the fourth and third terms, respectively, in Eq. 4 (approximated in Table 5 in the Appendix using a dusty-gas

relationship, see "Discussion" section). As fines are added to the collapsing mixture, even though the overall particle concentration stays the same, the behavior of the coarse particles is "pulled" towards that of the fines, and they are able to better follow the velocity changes in the gas (dusty-gas) upon impact. This phenomenon means that a fines-rich mixture is likely to produce an outgoing flow that is dilute using the criterion in this paper, all other factors being equal (Fig. 2a), even though the total particle concentrations will be elevated compared with the impacting mixture. Recall that bulk particle densities between ~ 100 and 400 kg/m³ ($\epsilon_{tot} \approx 0.05$ to 0.2) would be in the transitional regime described above with formation and settling of particle clusters (Weit et al. 2018, 2019).

Effects of concentration and speed of collapsing mixture

Intuitively, one might expect that impacting mixtures with higher ϵ_{tot} would be more likely to produce concentrated outgoing flows, especially if they have high proportions of coarse particles. This is indeed the case, but with the added complexity of compressible flow phenomena, which become important at higher speeds and/or higher fine particle
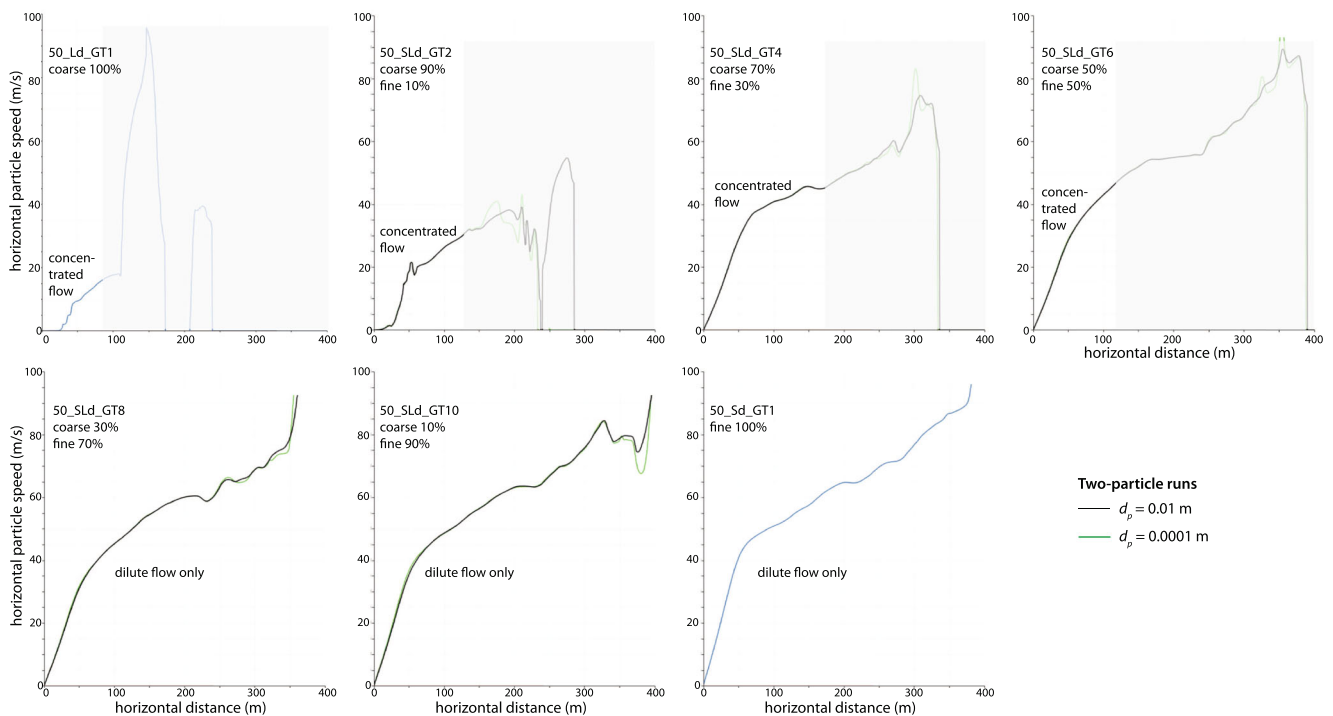
Fig. 4 Effect of proportions of coarse and fine particles in impacting flow on horizontal particle speed along the ground of the resulting lateral flows, for the same simulations shown in Fig. 3. "Distal" parts of the plots record an initial jet with high speeds, caused by displacement of air upon initial impact of the collapsing mixture, which is not of interest to this study, and are also affected by the expulsion flow that occurs when coarse particles are abundant. Also note that the high speeds in the right part of each plot are mainly gas (with some particles; compared with corresponding plots in Fig. 3). An extreme example is the coarse-only run (upper left), where the particle concentration drops towards zero beyond $x \approx 120$ m; the high speeds beyond that distance (the largest a result of gas expulsion at impact) are essentially pure gas although numerically, a very small particle concentration is computed. Particle speed increases from zero at the center of the impact zone (between $x = 0, 25$ m), which is a stagnation point. Concentrated flows are slowest where the bulk density (particle concentration) is highest, i.e., for very coarse-rich cases, partly a simple reflection of continuity

concentrations. Comparing cases with equal proportions of coarse and fine particles and all other parameters, the same except ϵ_{tot} reveals that when $\epsilon_{tot} = 0.1$, a concentrated underflow formed but its concentration (bulk density; Fig. 5a) varied laterally due to expansion and recompression of the gas phase. In this case, the impacting flow was supersonic (Mach number 1.25; Table 5 in the Appendix), as was the proximal outgoing flow. The very dilute flow (ϵ_{tot} 0.001 in the 50 m/s impacting mixture) produced a dilute lateral flow, although the particle concentration along the ground was ~ 0.02–0.04, concentrated by more than a factor of ten compared with the impacting flow. Note that in the intermediate case of $\epsilon_{tot} = 0.01$ (center cases in Fig. 5a, b; see also Figs. 3 and 4), the leading edge of concentrated flow is indicated at ~ 120-m distance, but beyond that to a distance of ~ 220 m, the flow is just below the criterion I use in this paper and for practical purposes could be considered concentrated.

Gas pressure (P_g) is affected by the overall particle concentration (Fig. 5b). The $\epsilon_{tot} = 0.1$ supersonic case produced a very high pressure ($P_g \approx 9 \times 10^5$ Pa) at the impact zone, which decreased outward to slightly less than 10^5 Pa (ambient pressure), then it increased again as the mixture recompressed. When the impacting mixture had $\epsilon_{tot} = 0.01$, the concentrated underflow maintained a gas pressure between 2 and 9 kPa higher than ambient pressure. This excess pressure (compared with ambient) is a pore pressure, which is critical for mobility of concentrated flows (Roche 2012; Roche et al. 2016), and is in part inherited from the high values of P_g attained at the impact zone due to flow stagnation. When the impacting mixture's $\epsilon_{tot} = 0.001$, gas pressure was only slightly elevated in the most proximal part of the outgoing dilute flow.

In addition to the proportions of coarse and fine particles and the total particle concentration, impact speed affects the outgoing flow properties. A simulation with impact speed of 100 m/s, with equal proportions of coarse and fine particles and $\epsilon_{tot} = 0.01$, produced an outgoing flow with bulk densities between 260 and 426 kg/m³ (particle concentrations of 10–15 vol.%; Fig. 5a). This is below the concentrated-flow threshold use in this paper, unlike the simulation of the same conditions but impact speed of 50 m/s. Although the 100 m/s case is subsonic, its Mach number (0.84) is close enough to unity (Table 5 in the Appendix) that the lateral flow emerged from the impact zone as an overpressured flow that expanded and recompressed as it traveled outward (Fig. 5b). As discussed above, these compressible flow effects influence the particle concentration of the lateral flow. Concentrated lateral flows
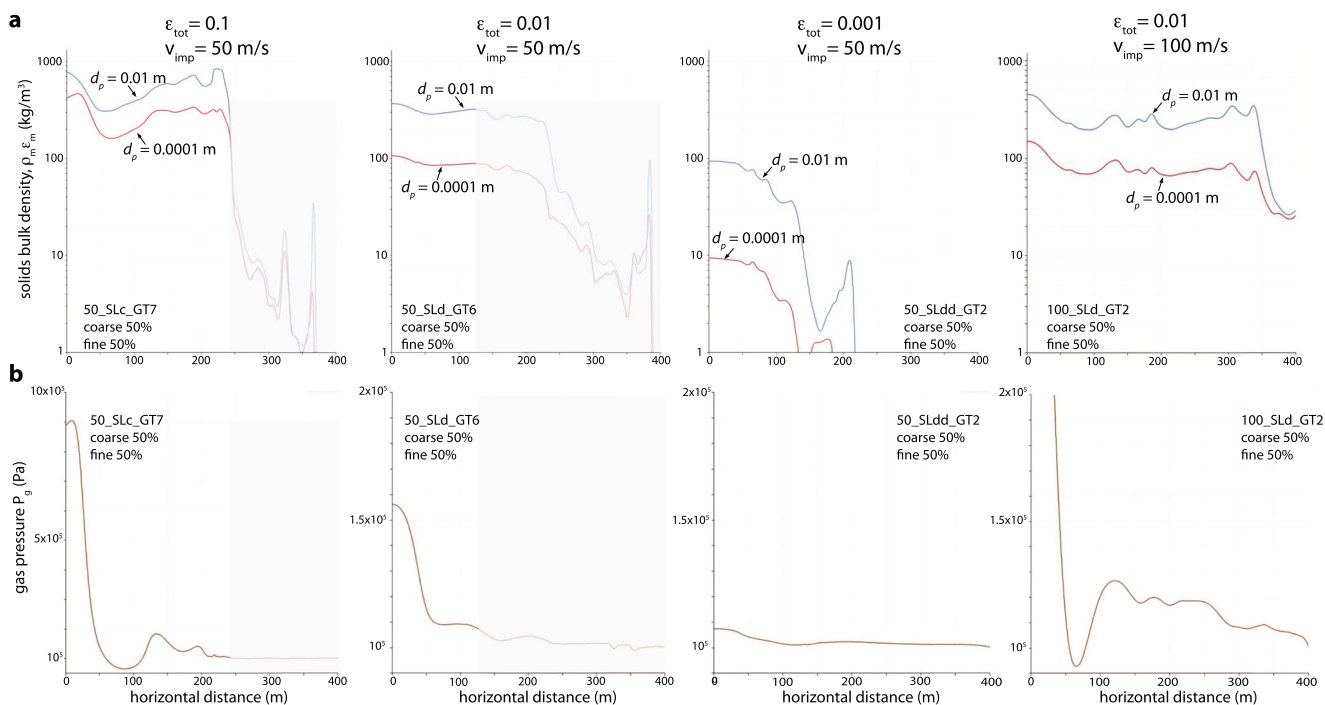
Fig. 5 Bulk solids (particle) densities (**a**) and gas pressure P_g (**b**) along the ground for different impacting particle concentrations (ϵ_{tot} = 0.1, 0.01, and 0.001) at t = 6 s and impact speed (v_{imp}) of 50 m/s (first three columns). In all three cases, the particles are 50% coarse and 50% fine in the impacting mixture. The first two cases form thin concentrated underflows (left of the shaded areas on the two plots). For the ϵ_{tot} = 0.1 case, bulk density and P_g first decrease then increase with distance; this is due to the expansion-recompression structure of the flow and the supersonic condition of the impacting mixture (Valentine and Sweeney 2018). Note the different P_g scale for this case, compared with the other two. For the ϵ_{tot} = 0.01 case, the bulk densities are near the threshold for concentrated versus

dilute flow used in this paper (ϵ_{tot} = 0.2), meeting the criterion for concentrated flow to a distance of 120 m but being just lower than that threshold to a distance of ~ 250 m. Gas pressure in that case decreases away from the 25-m-wide impact zone, maintaining values of ~ 2–9 kPa above ambient pressure (100 kPa). This represents a pore pressure in the concentrated underflow. For the ϵ_{tot} = 0.001 case, the outgoing flows are fully dilute. Far right plots are for ϵ_{tot} = 0.01 but with v_{imp} = 100 m/s; maximum P_g in the impact zone for this run is 3.3×10^5 Pa. Note in all cases that the coarse particles are concentrated relative to the fine ones, compared with their 50–50 mix in the impacting mixtures

for the 100 m/s impact speed cases required coarse fractions of 60% or greater of the total particle population (Table 5 in the Appendix).

Discussion

The results provide useful insights into the proximal dynamics of pyroclastic currents produced by collapsing gas-particle mixtures, but it is important to keep in mind some aspects in addition to the caveat described above about numerical resolution of the thin, concentrated underflows. First, all of the results are compared at times of 6 s after initiation of downward flow into the domain. This is obviously a short time frame compared with the duration of a sustained eruptive fountain, which might continue for many minutes to a few hours or tens of hours in the case of large ignimbrite-producing eruptions (Wilson and Hildreth 1997; Roche et al. 2016). If a collapsing mixture impacted the same location for an extended period, the coarse material might accumulate at the impact zone and produce outgoing concentrated flows that

develop over time. On the other hand, previous numerical modeling suggests that eruptive fountains vary in height and impact location with time, even if the discharge and particle size at the vent are constant, due to complex interactions with the ambient air and flow-back of material towards the vent (e.g., Valentine et al. 1992; Dobran et al. 1993; Neri and Dobran 1994). Thus, even for a sustained discharge, it may be unlikely that an impact zone would be stationary, especially because the fountaining particle size/density distribution in a real eruption can also be highly transient (e.g., due to wall rock avalanches into vents), so that the short time frames studied here would be applicable as the zone migrates laterally.

Second, the simulations all have the extreme case of vertical collapse and horizontal "ground," maximizing the changes in velocity associated with impact. In nature, the collapsing mixtures might approach the ground at an angle different from vertical, tilting back towards the fountain tops from which they originate. More importantly, though, many mixtures will impact sloping ground, especially in cases involving stratovolcanoes. This will modify the denominator in the impact Stokes number (fluid change time scale) to $t_f = \frac{\delta}{v_{imp}(1-sin\alpha)}$.

where α is the slope angle from horizontal, assuming that the deceleration length scale δ is unaffected by the slopes of interest here (up to $\sim 30°$). The flat-ground case modeled here is important to understand before adding complexity such as that related to topography, and the simulations are reasonable approximations for impacting mixtures around many calderas which have variable surrounding slopes or very shallow slopes due to previous ignimbrite eruptions.

Two additional points are the following: (1) The plots (Figs. 3, 4, and 5) represent conditions close to the ground, reflecting the focus in this paper. Concentrations, proportions of fine and coarse particles, and particle speeds vary widely above this basal region in any given simulation and are mostly within the dilute regime as defined here. (2) All of the simulations here use a half-width of 25 m for the collapsing mixture, which would correspond to a 50-m-wide downward flow from an eruptive fountain. Limited tests with different half-widths indicate that the lateral extents of parameter values (for example, distance of concentrated flow or elevated gas pressure) roughly scale with the half-width of the impacting mixture, consistent with other studies of impinging jets (e.g., Carling and Hunt 1974; Valentine and Sweeney 2018).

Particle distributions and relation to natural pyroclastic currents

Equations 3 and 4 and relevant constitutive models (Table 2 in the Appendix) describe in detail the momentum transfer (drag) between particles and gas and between particle classes. As mentioned above, the drag of fine particles exerted on coarse particles tends to draw the coarse particles towards the behavior of fine particles in the gas. This can be approximated in dilute regimes by treating the mixture of fines and gas as a single dusty-gas phase (a.k.a. pseudofluid; Marble 1970), such that the coarse particles interact with a dusty-gas that has higher density and viscosity than the pure gas in computing the particle response time scale ("Introduction" section):

$$\rho_{dg} = \left(\epsilon_{g(eff)} \rho_g \right) + \left(\epsilon_{f(eff)} \rho_f \right) \quad , \tag{9}$$

$$\mu_{dg} = \mu_g \left(1 + \frac{\epsilon_{f(eff)} \rho_f}{\epsilon_{g(eff)} \rho_g} \right)^2 \quad . \tag{10}$$

Here, the (*eff*) subscript indicates that only the gas and fines are used in computing their bulk densities for Eqs. 9 and 10, i.e., $\epsilon_{f(eff)} = \frac{\epsilon_f}{1 - \epsilon_c}$ and similarly for the gas fraction. The effects of Eqs. 9 and 10 are included in the impact Stokes numbers listed for each simulation in Table 5 in the Appendix.

Although all of the simulations reported here used some combination of 1-cm and 0.1-mm particles, both with material

densities of 2000 kg/m³, the impact Stokes numbers are applicable to other particle size-density combinations. The relationship between diameter and density for particles with the same measure of response time t_p is

$$\frac{d_2}{d_1} \approx \left(\frac{\rho_1}{\rho_2} \right)^{1/2} \quad , \tag{11}$$

where the subscripts 1 and 2 represent particle classes, assuming the gas or dusty-gas density is much smaller than the particle densities. Thus, the 1 cm diameter, 2000 kg/m³ particles used as the coarse field here are equivalent to $\sim$ 2-cm-diameter particles with pumice-like densities of 500 kg/m³. Similarly, the response time measures for particles with similar densities but different diameters, in the same dusty-gas, can be compared:

$$\frac{t_{p2}}{t_{p1}} \approx \left(\frac{d_{p2}}{d_{01}} \right)^2 \quad . \tag{12}$$

Thus, a 10-cm clast will have a t_p that is 100 times that of a 1-cm clast of the same density in the same dusty-gas. For example, in run 50_SLd_GT10, the 1-cm particles have $St_{imp} = 2.8$, but a 10-cm particle would have $St_{imp} = 280$, which is the same magnitude as in the coarse-only run of that series (50_Ld_GT1; see Table 5 in the Appendix). The 10-cm particles would be expected to form a concentrated underflow upon impact, though the 1-cm particles did not.

Breard et al. (2018, 2019b) pointed out the importance of the Sauter mean particle size in the transport dynamics of pyroclastic currents. The Sauter mean is the effective mean particle size in terms of the surface area for drag (and heat exchange) between particles and gas; it is the ratio of the total volume of particles to the total particle surface area (whether the particle sizes are monodisperse or polydisperse in a given mixture). Breard et al. (2019b) compiled grain size data from deposits of pyroclastic currents and computed the Sauter mean for each published analysis and showed how deposits of different types of currents (i.e., block and ash flow, small-volume pumice flow, large-volume ignimbrite-producing flow) each tend to have a typical value of Sauter mean. The simulations reported here have Sauter mean diameters ranging from 10,000 (coarse-only runs) to 100 μm (fines-only runs; see Table 5 in the Appendix), which can be compared with values of 250 to 50 μm from natural deposits (block-and-ash flow deposits and ignimbrites, respectively). Clearly, the coarse-rich (or coarse-only) simulations exaggerate the effect of low particle surface area relative to volume (or mass) fraction, compared with the data in Breard et al. (2019b), which is intentional. However, I note that the data analyzed by Breard et al. are individual samples, rather than whole-deposit grain size distributions; they are derived from the source mixture at the fountain (in the ignimbrite cases) but have been modified

by impact zone and transport processes, including ash production via abrasion, and by deposition. Dufek and Manga (2008) showed how a significant fraction (10–20 vol.%) of pumice lapilli can convert to ash by abrasion processes during lateral flow. Thus, an initially relatively coarse mixture of pumice and lithic coarse-ash to lapilli (and blocks) impacting the ground around an eruptive fountain could nucleate concentrated flows upon impact that become finer grained as they travel away and aggrade a deposit. Also note that a tremendous amount of abrasion must happen in the impact zone itself, suggesting that the total grain size distribution of the outgoing flow might be substantially weighted towards fines compared to the impacting mixture; this is a topic for future work. The Sauter mean values above do not include grain size data from proximal breccia deposits that are common in larger (greater than a few cubic kilometers) ignimbrites, and for which only partial granulometry has been measured due to the coarseness of the deposits (Druitt and Bacon 1986; Perrotta and Scarpati 1994). As noted below, such breccias likely record, at least in part, highly transient introduction of coarse and dense clasts into an eruptive mixture, suggesting that the grain size (and density) distribution of a mixture feeding a fountain would also be highly transient. The coarse-only simulations in this paper are likely reasonable for some portions of fountains during phases that involve large quantities of wall-rock debris being introduced into an eruptive jet.

Concentrated vs dilute pyroclastic currents from eruptive fountains (column collapse)

The results presented here provide some insights into conditions for which a pyroclastic current produced by fountaining is best approximated with a depth-averaged granular flow model or by a box model of dilute transport and sedimentation for hazards modeling purposes. The complexities and nonlinear coupling of many parameters in multiphase flows make standard scaling approaches, which could result in simple regime diagrams, elusive. However, for a given combination of impacting speed and total particle concentration, the formation of concentrated underflow at the impact zone is related to St_{imp} for the coarse particles and the flux per unit area of coarse particles into the impact zone (Fig. 6). For impacting mixtures with intermediate concentrations of about one to a few volume percent, and with relatively low Mach numbers, the numerical results indicate a rough boundary between scenarios that produce concentrated versus dilute-only lateral currents. The slope of the boundary indicates that as St_{imp} for the coarse particles decreases (for example, due to increasing proportion of fines), a larger flux per unit area of those particles is required to generate a concentrated underflow. Impacting mixtures with sufficiently high Mach numbers are affected by the expansion-recompression zones of the outgoing flow, therefore not behaving exactly as predicted by the rough regime

boundary (Fig. 6). Because all lateral flows that leave the impact zone are more concentrated than the impacting flows (typically by a factor of a few), impacting mixtures with sufficiently high values of ϵ_{tot} will always produce concentrated flows if they have some coarse particles (e.g., the impacting mixtures with $\epsilon_{tot} = 0.1$; Fig. 6). Within the range of parameters explored in this paper, for intermediate concentration, subsonic impacting mixtures whose parameters fall above the boundary on Fig. 6, a depth-averaged granular flow model could be used for the concentrated underflow (but keeping in mind that the overriding dilute flow could travel faster and farther than the underflow, potentially making a two-layer approach the best; Kelfoun 2017). The boundary condition for the source of the lateral flow could be a flux boundary condition. For highly concentrated collapsing mixtures (likely the case in most lava dome collapse scenarios), a depth-averaged granular flow approach is justified, but keeping in mind that compressible flow effects might add some complexity to the proximal flow field. Impacting mixtures with intermediate concentrations that fall below the rough boundary in Fig. 6 can be treated with a dilute flow model, also preferably using a flux boundary condition for the source (as in Shimizu et al. 2019). At very low impacting concentrations (likely when $\epsilon_{tot} < 10^{-3}$, approximately), outgoing flows will essentially always be dilute.

Unfortunately, there is no simple recipe for determining when the depth-averaged granular or the dilute box model approach is best for a column-collapse (fountain)-fed pyroclastic current; the choice requires some knowledge of expected eruption conditions and fountain processes. However, this work shows the factors, for a given scenario, that can inform the use of the different end-member types of hazards models. Even though a relatively small number of parameter combinations (out of an infinite set of combinations) were studied here, these combinations can guide model section for a wider range of scenarios. For example, a particle flux per unit area from a collapsing mixture of $q_{tot} = 1$ m^3/m^2 s (similar to simulations here, see Fig. 6), falling as a 50-m-wide "curtain" from a fountain with a radius of 300 m from a central vent (appropriate for a 500-m-high fountain fed by an exit speed of 100 m/s) would correspond to a total dense-rock-equivalent volumetric eruptive flux of ~ 10^5 m^3/s. If ~ 10% of the erupting particles (coarse particle flux per unit area of ~ 0.1 m^3/m^2 s) have impact Stokes numbers greater than about 100, then concentrated currents are likely to be produced upon impact (Fig. 6). Finally, I note that concentrated underflows can originate not only upon impact but also farther downstream, sourced from dilute flows (examples of this were small concentrated flows produced by the 18 May 1980 lateral blast in valleys around Mount St. Helens, and from dilute ash-cloud surges at Soufrière Hills volcano, Montserrat; Fisher 1990; Druitt et al. 2002). This paper does not address such scenarios (but see Doyle et al. 2008; Shimizu et al. 2019).
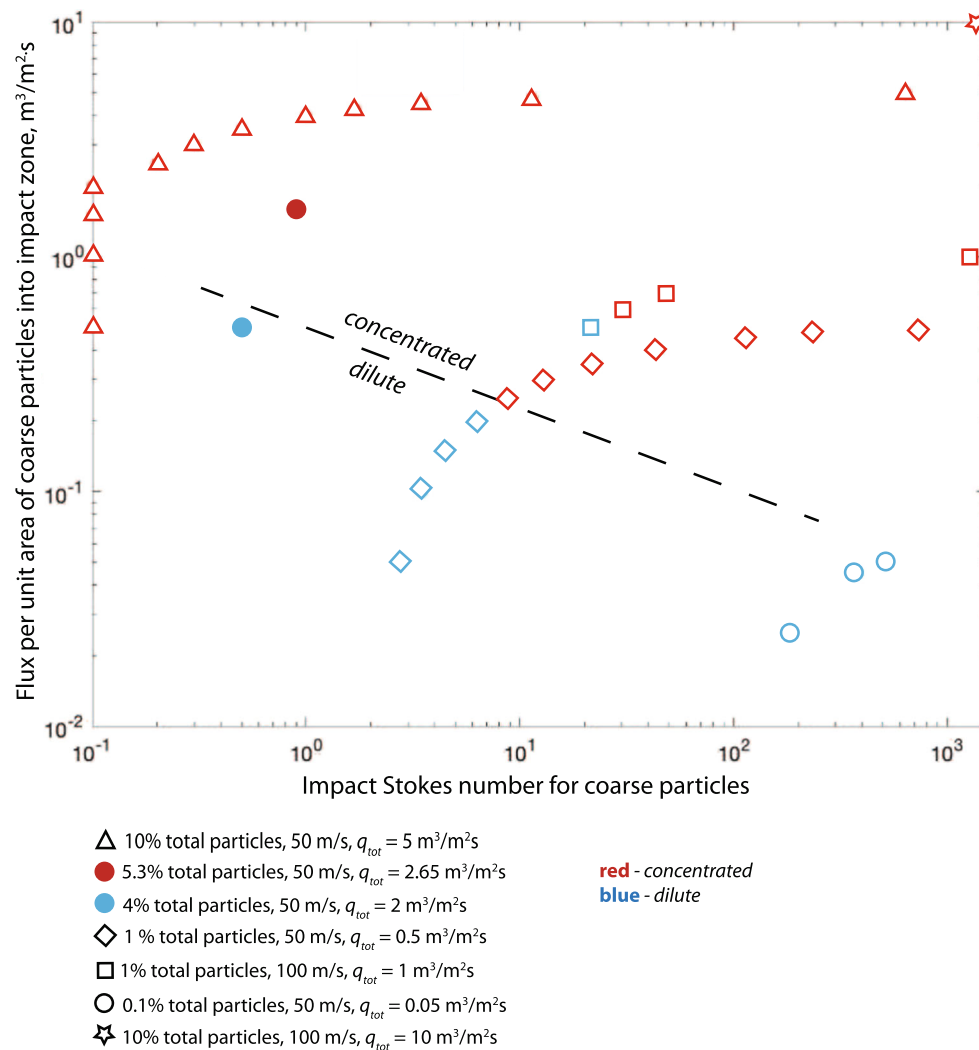
Fig. 6 Scatter plot of simulation results in terms of flux per unit area of coarse clasts to the impact zone ($v_{imp}\epsilon_c$) and impact Stokes numbers, with each point referring to a simulation (Table 5 in the Appendix). Different symbols represent impacting mixture properties (also defined in terms of the total particle flux per unit area to the impact zone, $q_{tot} = v_{imp}\epsilon_{tot}$). Dashed line indicates approximate boundary between conditions that produced concentrated underflows upon impact and those that produced dilute-only lateral flows, for cases with intermediate impacting particle concentrations. The outlier case (blue square above the dashed line, run 100_SLd_GT2; Table 5 in the Appendix, see also Fig. 5) produced lateral flow with bulk particle density ranging between 260 and 426 kg/m³; much of the outgoing flow was just below the threshold bulk density of 400 kg/m³ for identification as a concentrated flow in this paper, and the concentration of the outgoing flow was overprinted by compressible flow effects (Mach number of impacting mixture of 0.84)

Proximal breccia facies of ignimbrites

The numerical results presented here have implications for the development of proximal ignimbrite facies. Such deposits are often dominated by lithic clasts and dense juvenile components of decimeter to meter sizes (e.g., Wright and Walker 1977; Druitt and Bacon 1986; Yasuda and Suzuki-Kamata 2018); St_{imp} for these sizes can be compared, using Eq. 12, with those in the simulations (Table 5 in the Appendix) in order to extend the modeling results to those coarse clasts. Laterally, the proximal breccias can have complex internal stratigraphy and varied lateral and vertical relationships with more "normal" ignimbrite. For example, Druitt and Sparks

(1982) describe examples of steep internal contacts (cut and fill structures) between breccia units from a single eruption, especially where exposed along the caldera wall, in the Cape Riva deposits at Santorini. They also documented the occurrence of a dm-thick, reverse-graded, and crudely stratified horizon at the base of most breccia units at a given location. These basal horizons transition laterally to the reverse coarse-tail-graded bases of ignimbrites, as the breccias also grade laterally to ignimbrite. Druitt and Sparks (1982) concluded that the pyroclastic currents that produced these deposits were concentrated flows and that fines-depletion of the breccia deposits (relative to the ignimbrite into which they grade laterally) and the presence of fines-depleted pipes are consistent

with large gas fluxes during transport and deposition. Suzuki-Kamata and Kamata (1990) documented similar characteristics of proximal breccias in the Tosu ignimbrite, including the presence of both clast-supported (fines-depleted) and matrix-supported facies. Other studies documented similar characteristics (e.g., Druitt and Bacon 1986; Perrotta and Scarpati 1994; Bear et al. 2009; Yasuda and Suzuki-Kamata 2018), also showing that proximal breccias range in their relationships with pre-eruptive topography from crudely mantling to ponded in low areas. It is worth noting that many of the descriptions of proximal breccia facies are associated with deposits from caldera-forming eruptions and document locations along or near the source caldera rims. Such locations are potentially in the impact zones of collapsing columns erupted from caldera ring vents.

Modeling results presented here and in previous multiphase studies (Valentine and Wohletz 1989; Dartevelle et al. 2004; Sweeney and Valentine 2017; Valentine and Sweeney 2018) do not support the oft-cited deflation zone concept put forward by Walker (1985), wherein the lateral extent of lithic-rich breccias represents the lateral extent of a dilute current where lithic clasts preferentially settle first. Rather, coarse, dense lithic clasts concentrate immediately upon impact and propagate outward as concentrated underflows when they are present in sufficient proportions in the collapsing mixture. This mechanism for proximal breccia facies is similar to that initially conceptualized by Wright and Walker (1977), who inferred a "lag-fall" mechanism for the proximal breccias at the site of impact, although they do not discuss lateral flow of that concentrated mixture. Druitt and Sparks (1982) inferred similar processes and qualitatively discussed high gas pressures in the impact zone, also alluding to expulsion of gas and fines as described here.

The modeling suggests that many proximal breccias were produced by collapsing mixtures with large (generally 50 vol.% or more) proportions of high St_{imp} clasts. These clasts were introduced by wall-rock avalanches into vents, especially during caldera collapse, as inferred by many authors (see Aramaki 1984; Druitt 1985). Although it is common to think of ignimbrite-forming eruptions as steady, the process of lithic debris avalanching into vents must vary dramatically in both space and time. Likewise, at a given time and location, the impacting mixture might or might not have many high-St_{imp} clasts (keeping in mind that coarse juvenile clasts can also have high Stokes numbers). Complex lateral (both radial and circumferential) and vertical facies variations result, such as those described by Druitt and Sparks (1982), and variations in the fines contents of proximal breccias (Yasuda and Suzuki-Kamata 2018) can be related to different amounts of avalanche material combining with the eruptive mixtures.

A final note relates to observations of hummocks or mounds of coarse breccia (Fig. 7a; Druitt and Bacon 1986). Modeling shows that such features could be produced directly from impact of a coarse collapsing mixture. An extreme example is a coarse-only simulation with high total particle concentration of 10 vol.%. In such a case, the impacting mixture builds a mound of particles that thickens until its slopes are near the angle of repose, while particles flow down its outer slopes to feed a concentrated lateral flow and expelled gas jets over that granular flow (Fig. 7b). The mound is a simulated deposit, with both particle velocity and granular temperature being zero in its interior (Fig. 7 c, d); it has an elevated gas pressure that is close to that which would be predicted as a stagnation pressure for the impacting mixture (2.5×10^5 Pa), and which is highest along its upper portion where the mound top has become the impact surface for the falling mixture (Fig. 7e). The elevated gas pressure is carried outward in the thin, concentrated flow as a pore pressure (several kPa larger than ambient pressure). Thus, proximal mounds of breccia might record the temporary locations of impact zones, although there are likely additional mechanisms for their formation.

Conclusions

I have presented results of multiphase numerical modeling of impacting gas-particle mixtures, focusing on the implications for the resulting lateral flows which provide insights into the development of pyroclastic currents from eruption column collapse scenarios. Lateral flows are sensitive to impact speeds, overall particle concentrations, and proportions of fine and coarse particles. For $\epsilon_{tot} \approx 0.01$, an impacting mixture with up to approximately equal proportions of coarse and fine particle (or higher proportions of coarse) will tend to form a concentrated underflow which can be approximated by a depth-averaged granular flow model for hazard assessment purposes starting from the impact zone. Low total particle concentrations (e.g., $\epsilon_{tot} \approx 0.001$) tend to produce dilute lateral flows that could be simplified to box model approaches for dilute pyroclastic currents. Higher total concentrations produce concentrated lateral underflows but these can be complicated by Mach number effects. Higher impacting speeds, within the range studied here, require relatively larger proportions of coarse particles to form concentrated underflows. In general, some knowledge of the eruption column (fountain) conditions is required in order to make an informed decision as to which simplified hazards modeling approach is most applicable for a given scenario. While the emphasis in this paper is on ignimbrite-forming processes, these mechanisms in principle influence the characteristics of any type of pyroclastic current that is produced by a collapsing mixture, as well as the development of massive deposits focused in topographic lows (from concentrated currents) compared with stratified and cross-stratified, topography-draping deposits (from dilute currents).
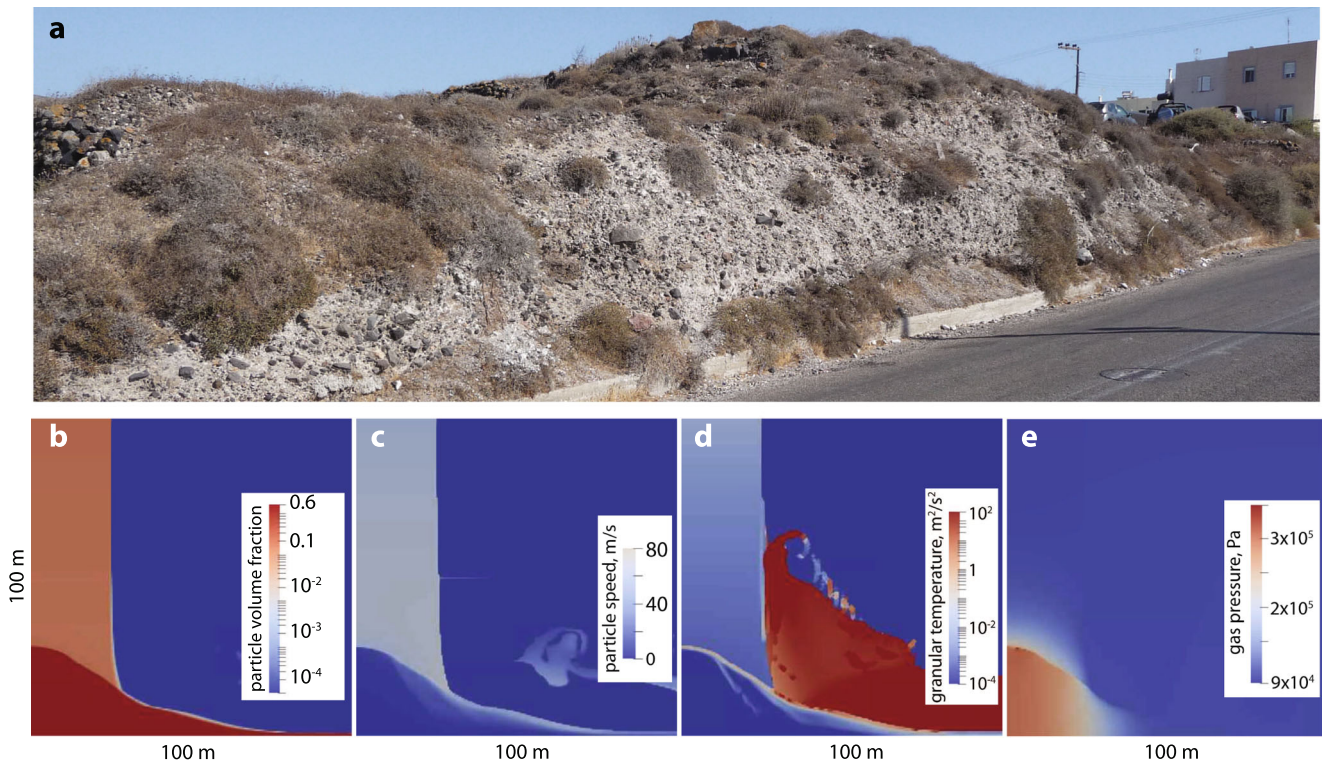
Fig. 7 **a** A mound of proximal breccia (Minoan eruption, Santorini, north side of Oia village; courtesy TH Druitt). **b–d** Snapshots of parameters in the proximity of simulated impact (out to 100 m horizontally) for the extreme case of an impacting flow consisting of a particle volume fraction of 0.1, entirely coarse particles, illustrating deposition analogous to a hummock as observed in natural proximal breccias (run 50_Lcart_GTb2, Table 5 in the Appendix). **b** Particle volume fraction (log scale). Dark red color represents maximum packing. **c** Magnitude of particle velocity, showing zero motion (deposit) within the maximum packing region except for its outer margin. As the deposit builds, particles flow down its margin to feed the lateral flow. **d** Granular temperature (log scale), showing negligible values within most of the maximum packing region, meaning essentially zero particle velocity fluctuations, consistent with a deposit. Note higher granular temperature on margins of the maximum packing region, consistent with shear as a source term in Eq. 10. **e** Gas pressure shows a large stagnation pressure within the deposit especially at its top, while pressures remain slightly elevated relative to ambient pressure within the lateral flow that extends to 116 m (beyond the portion of the domain shown here), consistent with pore pressure even in this coarse-grained case. Gas velocity (not shown) reaches values up to ~ 115 m/s immediately above the concentrated outgoing flow due to expulsion upon impact

Valentine et al. (2019) compared two ignimbrites with different abundances of poorly coupled, coarse clasts and discussed potential implications for overall ignimbrite facies; the results presented here provide additional insights into the formation of proximal breccia facies of ignimbrites. Modeling indicates that such breccias are related to influx of coarse wall-rock material into an eruptive mixture, which increases both the total particle concentration and the proportion of coarse dense clasts in the mixture that subsequently collapses and impacts the ground; these correspond to increases in the coarse particle flux per unit area at the impact zone and to increasing impact Stokes number of the coarse clasts (Fig. 6). The breccias record concentration of dominantly coarse clasts immediately upon impact and formation of concentrated flows that propagate laterally while expelled fines and gas flow rapidly outward as dilute currents. Lateral heterogeneity in proximal deposits likely records rapid time and space variations in avalanches of material into eruptive vents, and the occurrence of proximal breccia hummocks might record the temporary positions of impact zones.

The modeling shown in this paper covers a limited range of parameters and is simplified, particularly in that it only includes two particle sizes. However, the range of behaviors of the two sizes and their interactions with each other (for example, fine particles causing better coupling of large particles to the gas flow field and concentration of coarse particles causing expulsion of fines and gas) are reasonably representative of many natural mixtures. Similarly, the ranges of impact speeds and total particle concentrations capture a large part of the spectrum of values expected from fountaining eruptions. Thus, the results provide general insights into the initiation of pyroclastic currents from collapsing mixtures. Future work is needed to broaden the range of parameters, and in particular new numerical techniques which can model a thin granular region within (and coupled to) a large, three-dimensional flow field—while still honoring the continuum-like behavior of pyroclastic currents—would be beneficial. Especially valuable would be estimates of the source grain size and density distributions for natural

ignimbrite-forming eruptions. This is a more difficult determination than that of whole-deposit grain size distributions for fallout deposits (Bonadonna and Houghton 2005) due to the complexity of processes that modify the original distribution during impact, lateral transport, and deposition of pyroclastic current deposits. Tackling this problem would require application of some techniques used for fallout deposits, in order to get a whole-*deposit* characterization (e.g., Lube et al. 2007), but would additionally involve some inverse assessment of the modification processes during impact and transport and losses due to co-ignimbrite ash dispersal, as well as temporal variation related to magma properties, fragmentation, and transient introduction of lithic debris.

Appendix. Notation, constitutive models, initial and boundary conditions, and material properties

Table 1 Notation

Symbol	Definition; units
C_{DM}	Multiparticle drag coefficient
C_{fml}	Coefficient of friction between particles constituting the lth and m^{th} solid phases
C_{pg}	Specific heat of the gas; J/kg·K
C_{pm}	Specific heat of the mth phase; J/kg·K
d_{pm}	Diameter of the particles constituting the mth solid phase; m
e_{ml}	Coefficient of restitution for the collisions between particles constituting the lth and m^{th} solid phases
g_i	Acceleration due to gravity; m/s^2
g_{0ml}	Radial distribution function at contact for a mixture of hard spheres
i, j, k	Subscripts for identifying vector and tensor components; if there are multiple subscripts, these indices appear at the end of the list of subscripts and summation convention is implied only for these indices
I_{mli}	Momentum transfer between the mth and the lth phases due to interphase drag force; N/m^3
J_m	Collisional dissipation of granular temperature of mth phase; m^2/s^3
M	Total number of solid phases
P_g	Gas-phase pressure; Pa
P_c	Solid-phase pressure in close-packed regions; Pa
q_{gj}	Conductive heat flux in the gas; J/m^2·s
q_{mj}	Conductive heat flux in the mth phase; J/m^2·s
Re_m	Particle Reynolds number of the mth solid phase
St_{imp}	Stokes numbers for particles in impacting flows
t	Time; s
t_f	Time scale for fluid velocity changes in Stokes number; s
t_p	Time scale for particle response to fluid velocity changes in Stokes number; s
T_g	Thermodynamic temperature of the gas; K
T_m	Thermodynamic temperature of the mth phase; K
T_{Rm}	Background temperature in a radiation model; K
U_{mj}	J^{th} component of the mth phase velocity; m/s
U_{gj}	J^{th} component of the gas velocity; m/s
v_{imp}	Impact speed (vertical); m/s
x_j	J^{th} coordinate direction; m
γ_{gm}	Gas-solid heat transfer coefficient; J/m^3·K·s

Table 1 (continued)

Symbol	Definition; units
γ_{Rm}	Radiative heat transfer coefficient for the mth phase; J/m^3·K^4·s
δ	Length scale for fluid velocity changes in Stokes number; s
δ_{ij}	Kronecker delta; 0 if $i \neq j$, 1 if $i = j$
ϵ^*	Void fraction (or gas volume fraction) of close-packed solids
ϵ_{sf}^{min}	Minimum particle volume fraction for frictional stress model
ϵ_c	Volume fraction of coarse particles
ϵ_f	Volume fraction of fine particles
ϵ_g	Volume fraction of gas
ϵ_m	Volume fraction of the mth phase
ϵ_{tot}	Total volume fraction of particles (coarse plus fine)
κ_m	Conductivity of granular temperature; kg/m·s
Π_m	Dissipation of granular temperature via gas-particle drag; kg/m·s^3
Θ_m	Granular temperature of the mth phase; m^2/s^2
ρ_{dg}	Density of a dusty-gas for particle time scale in Stokes number; kg/m^3
ρ_f	Material density of the fine particles for use in dusty-gas approximation; kg/m^3
ρ_m	Material density of the mth phase; kg/m^3
ρ_g	Density of the gas phase; kg/m^3
ρ_p	Particle density in Stokes number
τ_{gij}	Stress tensor of the gas; Pa
τ_{mij}	Stress tensor of the mth phase; Pa
τ_{mij}^f	Frictional component of the stress tensor of the mth phase; Pa
τ_{mij}^k	Kinetic component of the stress tensor of the mth phase; Pa
μ_g, μ_{dg}	Gas or dusty-gas viscosity; Pa s

Table 2 Interphase drag (momentum transfer) relationships (Syamlal et al. 2017)

Gas-particle drag	$I_{gmi} = \frac{3}{4} \frac{C_{Dm}\epsilon_g\epsilon_m\rho_g}{d_{pm}} |\boldsymbol{u}_g - \boldsymbol{u}_m| (U_{gi} - U_{mi})$
	where,
	$C_{Dm} = \begin{cases} \dfrac{200(1-\epsilon_g)}{\epsilon_g^2 Re_m} + \dfrac{7}{3\epsilon_g}, & \epsilon_g \leq 0.8 \\[2ex] \dfrac{24}{\epsilon_g Re_m}\left(1 + 0.15(\epsilon_g Re_m)^{0.687}\right)\epsilon_g^{-2.65}, & \epsilon_g > 0.8, (\epsilon_g Re_m) < 1000 \\[2ex] 0.44\epsilon_g^{-2.65}, & \epsilon_g > 0.8, (\epsilon_g Re_m) \geq 1000 \end{cases}$
	$Re_m = \dfrac{d_{pm}|\boldsymbol{u}_g - \boldsymbol{u}_m|\rho_g}{\mu_g}$
Particle-particle drag	$I_{mli} = F_{ml}(U_{mi} - U_{li})$
	where
	$F_{ml} = 3(1 + e_{ml})\left(\dfrac{\pi}{2} + C_{fml}\dfrac{\pi^2}{8}\right)\dfrac{(d_{pm} + d_{pl})^2}{2\pi(\rho_m d_{pm}^3 + \rho_l d_{pl}^3)}\rho_m\rho_l g_{0ml}|\boldsymbol{u}_g - \boldsymbol{u}_m| + S_{coef}P_c$
	$g_{0ml} = \dfrac{1}{\epsilon_g} + \dfrac{3\left(\sum_{l=1}^{M}\frac{\epsilon_l}{d_{pl}}\right)d_{pl}d_{pm}}{\epsilon_g^2(d_{pl} + d_{pm})}$ (radial distribution function)

Table 3   Granular stress and granular temperature constitutive equations (from Eqs. B4–13, C7–11 of Benyahia et al. 2012; see also Breard et al. 2019a)

Kinetic stress	$\tau^k_{mij} = \left(-P_m + \eta\mu_b \frac{\partial U_{mi}}{\partial x_j}\right)\delta_{ij} + 2\mu_m S_{mij}$

$$S_{mij} = \frac{1}{2}\left(\frac{\partial U_{mi}}{\partial x_j} + \frac{\partial U_{mj}}{\partial x_i}\right) - \frac{1}{3}\frac{\partial U_{mi}}{\partial x_i}$$

$$P_m = \epsilon_m \rho_m \Theta_m \left[1 + 4\eta \sum_{n=1}^{M} (\epsilon_n g_{0,mn})\right] \text{ where } \eta = \frac{1+e_m}{2}$$

$$\eta = \frac{1+e}{2}$$

$$\mu_m = \left(\frac{2+\alpha}{3}\right)\left[\frac{\mu^*_m}{g_{0,mn}\eta(2-\eta)}\left(1 + \frac{8}{5}\eta\sum_{n=1}^{M}(\epsilon_n g_{0,mn})\right)\left(1 + \frac{8}{5}\eta(3\eta-2)\sum_{n=1}^{M}(\epsilon_n g_{0,mn})\right) + \frac{3}{5}\eta\mu_b\right]$$

with $\alpha = 1.6$ (Agrawal et al. 2001)

$$\mu = \frac{5}{96}\rho_m d_{pm}\sqrt{\pi\Theta_m}$$

$$\mu^*_m = \frac{\rho_m \epsilon_m g_{0,mn}\Theta_m \mu}{\rho_m \sum_{n=1}^{M}(\epsilon_n g_{0,mn})\Theta_m + \left(\frac{2\beta\mu}{\rho_m\epsilon_m}\right)}$$

$$\beta = \frac{3}{4}C_{Dm}\frac{\rho_g \epsilon_g \epsilon_m |U_g - U_m|}{d_{pm}\epsilon_g^{2.65}}$$

$$\mu_b = \frac{256}{5\pi}\mu\epsilon_m \sum_{n=1}^{M}(\epsilon_n g_{0,mn})$$

Frictional stress	$\tau^f_{mij} = -P_{fm}\delta_{ij} + 2\mu_f \boldsymbol{S}$

$$P_{fm} = P_c\left(1 - \frac{\nabla\cdot\boldsymbol{v}_m}{n\sqrt{2}\sin(\phi)\sqrt{\boldsymbol{S_m}:\boldsymbol{S_m}+\Theta_m/d_{pm}^2}}\right)^{n-1}\frac{\epsilon_m}{\epsilon_{tot}}$$

$$P_c = \begin{cases} 10^{24}(\epsilon^* - \epsilon_g)^{10} & \epsilon_g < \epsilon^* \\[2mm] 0.05\frac{\left[(1-\epsilon_g)-\epsilon_{sf}^{min}\right]^2}{(\epsilon_g - \epsilon^*)^5} & \epsilon^* \leq \epsilon_g < \left(1-\epsilon_{sf}^{min}\right) \\[2mm] 0 & \epsilon_g \geq \left(1-\epsilon_{sf}^{min}\right) \end{cases}$$

$$\mu_{fm} = \frac{\sqrt{2}P_{fm}\sin\phi}{\sqrt{\boldsymbol{S}:\boldsymbol{S}+\Theta_m/d_{pm}^2}}\left(n-(n-1)\left(\frac{P_{fm}}{P_c}\right)^{\frac{1}{n-1}}\right)\frac{\epsilon_m}{\epsilon_{tot}}$$

$$n = \begin{cases} \frac{\sqrt{3}}{2\sin\phi} & \nabla\cdot\boldsymbol{v}_m \geq 0 \\[2mm] 1.03 & \nabla\cdot\boldsymbol{v}_m < 0 \end{cases}$$

where $\boldsymbol{v}_m$ is the solid phase m velocity vector in frictional regime, $\boldsymbol{S_m}$ is tensor form of S_{mij} in frictional regime, and ϕ is internal friction angle.

Granular temperature	

$$\kappa_m = \frac{\kappa^*_m}{g_{0,mn}}\left[\left(1 + \frac{12}{5}\eta\sum_{n=1}^{M}(\epsilon_n g_{0,mn})\right)\left(1 + \frac{12}{5}\eta^2(4\eta-3)\sum_{n=1}^{M}(\epsilon_n g_{0,mn})\right) + \frac{64}{25\pi}(41-33\eta)\eta^2\left(\sum_{n=1}^{M}(\epsilon_n g_{0,mn})\right)\right]$$

$$\kappa^*_m = \frac{\rho_m \epsilon_m g_{0,mn}\Theta_m \kappa}{\rho_m \sum_{n=1}^{M}(\epsilon_n g_{0,mn})\Theta_m + \left(\frac{6\beta\kappa}{5\rho_m\epsilon_m}\right)}$$

$$\kappa = \frac{75\rho_m d_{pm}\sqrt{\pi\Theta_m}}{48\eta(41-33\eta)}$$

$$J_m = \frac{48}{\sqrt{\pi}}\eta(1-\eta)\frac{\sum_{n=1}^{M}(\epsilon_n g_{0,mn})}{d_{pm}}\Theta_m^{3/2}$$

$$\eta = \frac{1+e}{2}$$

$$\Pi_m = -3\beta\Theta_m + \frac{81\epsilon_m\mu_g^2|\boldsymbol{u}_g - \boldsymbol{u}_m|^2}{g_{0,mn}d_{pm}^3\rho_m\sqrt{\pi\Theta_m}}$$

Table 4 Initial and boundary conditions, and material properties common to all simulations

Domain size	• 100 m high, 400 m wide unless noted
Boundary conditions (except inlet)	
• Left side	• Free slip wall
• Top	• Outflow (except inlet)
• Inlet	• Mass inflow (see Table 4)
• Right side	• Outflow
• Bottom	• Partial slip boundary (Johnson and Jackson 1987)
Inlet conditions	
• Gas pressure	• 10^5 Pa
• Inlet width	• 25 m
• Temperature (gas and particles)	• 293.15 K
• Granular temperature[1]	• 0.01 m^2/s^2
Computational grid	Uniform, $\Delta x = \Delta y = 0.5$ m
Initial conditions	
• Gas	• Air
• Gas pressure	• 10^5 Pa
• Temperature	• 293.15 K
• Particle concentration	• Zero
• Gas properties (air)	Burcat and Ruscic (2005) thermochemical database
Particle properties	
• Density	• 2000 kg m^{-3}
• Heat capacity	• 954.0 J kg^{-1} K^{-1}
• Coefficient of restitution	• 0.5
• Coefficient of friction between particles of two particle classes	• 0.5
• Specularity coefficient (for partial slip boundary)[1]	• 0 (sphere)
• Angle of internal friction[1]	• 28°
• Angle of internal friction at wall[1]	• 12°
• Maximum packing volume fraction	• 0.64

[1] Following Breard et al. (2019a), noting that granular temperature results in the flow field are insensitive to the boundary value (see also Dartevelle et al. 2004)

Table 5 Inlet conditions for simulations used in this paper

Run name	Inlet speed (m/s)	Inlet particle volume fraction	Particle size (and volume fraction) at inlet [1]	Sauter mean diameter (μm) [1]	Impact length scale (m) [2]	Impact Stokes number [3]	Impacting mixture sound speed [4] (m/s)	Inlet Mach number	Coarse particle impact flux $\epsilon_c v_{imp}$ (m³ particles/m²s)	Concentrated flow front at t = 6 s (m from jet center) [5]
50_Lcart_GTb2	50	0.10	10^{-2} m (0.10)	10^4	48	643	340	0.15	5.0	116
50_SLc_GT1	50	0.10	10^{-4} m (0.005) / 10^{-2} m (0.095)	1700	26	0.1 / 11.4	125	0.4	4.75	204
50_SLc_GT2	50	0.10	10^{-4} m (0.01) / 10^{-2} m (0.09)	917	23	0.1 / 3.5	89	0.56	4.5	220
50_SLc_GT3	50	0.10	10^{-4} m (0.015) / 10^{-2} m (0.085)	630	22	0.1 / 1.7	72	0.69	4.25	229
50_SLc_GT4	50	0.10	10^{-4} m (0.02) / 10^{-2} m (0.08)	481	21	0.1 / 1.0	63	0.79	4.0	230
50_SLc_GT5	50	0.01	10^{-4} m (0.03) / 10^{-2} m (0.07)	333	20	0.2 / 0.5	51	0.98	3.5	228
50_SLc_GT6	50	0.01	10^{-4} m (0.04) / 10^{-2} m (0.06)	246	19	0.2 / 0.3	44	1.14	3.0	238
50_SLc_GT7	50	0.01	10^{-4} m (0.05) / 10^{-2} m (0.05)	200	19	0.2 / 0.2	40	1.25	2.5	243
50_SLc_GT8	50	0.10	10^{-4} m (0.06) / 10^{-2} m (0.04)	166	19	0.2 / 0.1	36	1.39	2.0	253
50_SLc_GT9	50	0.10	10^{-4} m (0.07) / 10^{-2} m (0.03)	142	19	0.2 / 0.1	33	1.52	1.5	266
50_SLc_GT10	50	0.10	10^{-4} m (0.08) / 10^{-2} m (0.02)	125	19	0.2 / 0.1	31	1.61	1.0	270
50_SLc_GT11	50	0.10	10^{-4} m (0.09) / 10^{-2} m (0.01)	111	19	0.2 / 0.1	30	1.67	0.5	280
50_Sc_GT1	50	0.10	10^{-4} m (0.10)	100	19	0.2	28	1.79	0	N/A
50_Ld_GT1	50	0.01	10^{-2} m (0.01)	10^4	42	735	340	0.15	0.5	83
50_SLd_GT1	50	0.01	10^{-4} m (0.0005) / 10^{-2} m (0.0095)	1700	39	0.1 / 235	220	0.23	0.475	128
50_SLd_GT2	50	0.01	10^{-4} m (0.001) / 10^{-2} m (0.009)	917	38	0.1 / 114	187	0.27	0.45	127
50_SLd_GT3	50	0.01	10^{-4} m (0.002) / 10^{-2} m (0.008)	481	38	0.1 / 43	189	0.27	0.4	150
50_SLd_GT4	50	0.01	10^{-4} m (0.003) / 10^{-2} m (0.007)	333	39	0.1 / 22	154	0.32	0.35	171
50_SLd_GT5	50	0.01	10^{-4} m (0.004) / 10^{-2} m (0.006)	246	40	0.1 / 13	133	0.38	0.3	185
50_SLd_GT6	50	0.01	10^{-4} m (0.005) / 10^{-2} m (0.005)	200	41	0.1 / 8.6	119	0.42	0.25	120
50_SLd_GT7	50	0.01	10^{-4} m (0.006) / 10^{-2} m (0.004)	166	41	0.1 / 6.2	106	0.47	0.20	N/A
50_SLd_GT8	50	0.01	10^{-4} m (0.007) / 10^{-2} m (0.003)	142	42	0.1 / 4.5	101	0.50	0.15	N/A

Table 5 (continued)

Run name	Inlet speed (m/s)	Inlet particle volume fraction	Particle size (and volume fraction) at inlet	Sauter mean diameter (μm)[1]	Impact length scale (m)[2]	Impact Stokes number[3]	Impacting mixture sound speed[4] (m/s)	Inlet Mach number	Coarse particle impact flux $\epsilon_c v_{imp}$ (m³ particles/ m²s)	Concentrated flow front at t = 6 s (m from jet center)[5]
50_SLd_GT9	50	0.01	10^{-4} m (0.008), 10^{-2} m (0.002)	125	42	0.1 / 3.5	94	0.53	0.10	N/A
50_SLd_GT10	50	0.01	10^{-4} m (0.009), 10^{-2} m (0.001)	111	43	0.1 / 2.8	89	0.57	0.05	N/A
50_Sd_GT1	50	0.01	10^{-4} m (0.01)	100	43	0.1	84	0.60	0	N/A
50_Ldd_GT1	50	0.001	10^{-2} m (0.001)	10^4	59	523	340	0.15	0.05	N/A
50_SLdd_GT1	50	0.001	10^{-4} m (0.0001), 10^{-2} m (0.0009)	917	59	0.1 / 385	307	0.16	0.045	N/A
50_SLdd_GT2	50	0.001	10^{-4} m (0.0005), 10^{-2} m (0.0005)	200	50	0.1 / 185	233	0.21	0.025	N/A
50_Sdd_GT2	50	0.001	10^{-4} m (0.001)	100	54	0.1	188	0.27	0	N/A
100_Lc_GT2[6]	100	0.1	10^{-2} m (0.1)	10^4	44	1404	340	0.29	10.0	236
100_Ld_GT1	100	0.01	10^{-2} m (0.01)	10^4	48	1287	340	0.29	1.0	108
100_SLd_GT2[6]	100	0.01	10^{-4} m (0.005), 10^{-2} m (0.005)	200	33	0.2 / 21.3	119	0.84	0.5	N/A
100_SLd_GT3[6]	100	0.01	10^{-4} m (0.004), 10^{-2} m (0.006)	246	34	0.2 / 30.7	133	0.75	0.6	194
100_SLd_GT4[6]	100	0.01	10^{-4} m (0.003), 10^{-2} m (0.007)	333	35	0.2 / 48.7	154	0.65	0.7	312
50_SLint_GT1	50	0.04	10^{-4} m (0.03), 10^{-2} m (0.01)	133	23	0.01 / 0.5	50	1.0	0.5	N/A
50_SLint_GT2	50	0.053	10^{-4} m (0.021), 10^{-2} m (0.032)	246	23	0.1 / 0.9	60	0.83	1.6	225

Note. All runs are two-dimensional, Cartesian coordinates. Inlet width, 25 m; gas pressure, 10^5 Pa; inlet temperatures, 293.15 K (applies to both gas and particle fields)

[1] Sauter mean diameter computed according to Breard et al. (2019a)

[2] Length scales for deceleration above impact zone record the height at which the gas speed in the impacting mixture reaches 90% of the inlet speed at t = 6 s. These values are snapshots in time for a parameter that fluctuates to varying degrees (see Sweeney and Valentine 2017)

[3] Based on properties of air (assuming c_p = 1000 J kg^{-1} K^{-1}, c_v = 718 J kg^{-1} K^{-1}, plus concentration of fine particles in polydisperse runs are computed with dusty-gas properties for the carrier fluid composed of gas plus fine particles (Marble 1970)

[4] For cases where the bulk density of fine particles (particle density times fine particle volume fraction) is close to or less than the gas bulk density of the mixture, sound speed is computed using a dusty-gas relation (Marble 1970). For larger fine particle bulk densities, the relationship of Gidaspow (1994, p. 141) is used for sound speed

[5] Distances measured at t = 6 s; N/A means no concentrated flow formed by 6 s

[6] Used a 200-m-high computational domain to minimize interaction of gas flow with boundary in 100-m-high domain due to high velocities

References

Agrawal K, Loezos PN, Syamlal M, Sundaresan S (2001) The role of meso-scale structures in rapid gas-solid flows. J Fluid Mech 445: 151–185. https://doi.org/10.1017/S0022112001005663

Andrews BJ (2014) Dispersal and air entrainment in unconfined dilute pyroclastic density currents. Bull Volcanol 76:852. https://doi.org/10.1007/200445-014-0852-4

Andrews BJ, Manga M (2011) Effects of topography on pyroclastic density current runout and formation of coignimbrites. Geology 39: 1099–1102

Andrews BJ, Manga M (2012) Experimental study of turbulence, sedimentation and coignimbrite mass partitioning in dilute pyroclastic density currents. J Volcanol Geotherm Res 225-226:30–44

Aramaki S (1984) Formation of the Aira caldera, southern Kyusu, 22,000 years ago. J Geophys Res 89:8485–8501

Baer EM, Fisher RV, Fuller M, Valentine G (1997) Turbulent transport and deposition of the Ito pyroclastic flow – determinations using anisotropy of magnetic susceptibility. J Geophys Res Sol Earth 102:22565–22586

Bear AN, Cas RAF, Giordano G (2009) The implications of spatter, pumice and lithic clast rich proximal co-ignimbrite lag breccias on the dynamics of caldera forming eruptions: the 151 ka Sutri eruption, Vico volcano, Central Italy. J Volcanol Geotherm Res 181:1–24. https://doi.org/10.1016/j.jvolgeores.2008.11.032

Benyahia S, Syamlal M, O'Brien TJ (2012) Summary of MFIX Equations 2012–1. https://mfix.netl.doe.gov/download/mfix/mfix_current_documentation/MFIXEquations2012-1.pdf. Accessed 2 Oct 2019

Bonadonna C, Houghton BF (2005) Total grain-size distribution and volume for tephra-fall deposits. Bull Volcanol 67:441–456. https://doi.org/10.1007/s00445-004-0386-2

Branney MJ, Kokelaar P (2002) Pyroclastic density currents and the sedimentation of ignimbrites. Geol Soc Memoir 27

Breard ECP, Lube G (2017) Inside pyroclastic density currents – uncovering the enigmatic flow structure and transport behavior in large-scale experiments. Earth Planet Sci Lett 458:22–36. https://doi.org/10.1016/j.epsl.2016.10.016

Breard ECP, Lube G, Jones JR, Dufek J, Cronin SJ, Valentine GA, Moebis A (2016) Coupling of turbulent and non-turbulent flow regimes within pyroclastic density currents. Nat Geosci 9:767–774. https://doi.org/10.1038/NGEO2794

Breard ECP, Dufek J, Lube G (2018) Enhanced mobility of concentrated pyroclastic density currents: an examination of a self-fluidization mechanism. Geophys Res Lett 45:654–664. https://doi.org/10.1002/2017GL075759

Breard ECP, Dufek J, Roche O (2019a) Continuum modeling of pressure-balanced and fluidized granular flows in 2-D: comparison with glass bead experiments and implications for concentrated pyroclastic density currents. J Geophys Res Sol Earth 124:5557–5583. https://doi.org/10.1029/2018JB016874

Breard ECP, Jones JR, Fullard L, Lube G, Davies C, Dufek J (2019b) The permeability of volcanic mixtures – implications for pyroclastic currents. J Geophys Res Sol Earth 124:1343–1360. https://doi.org/10.1029/2018JB016544

Burcat A, Ruscic B. (2005) Third Millennium ideal gas and condensed phase thermochemical database for combustion with updates from active thermochemical tables. Report ANL-05/20 TAE 960, Argonne National Laboratory, Argonne, IL, USA

Burgisser A, Bergantz GW (2002) Reconciling pyroclastic flow and surge: the multiphase physics of pyroclastic density currents. Earth Planet Sci Lett 202:405–418

Bursik MI, Woods AW (1996) The dynamics and thermodynamics of large ash flows. Bull Volcanol 58:175–193

Carling JG, Hunt BL (1974) The near wall jet of a normally impinging, uniform, axisymmetric, supersonic jet. J Fluid Mech 66:159–176

Cas RAF, Wright HMN, Folkes CB, Lesti C, Porreca M, Giordano G, Viramonte JG (2011) The flow dynamics of an extremely large volume pyroclastic flow, the 2.08-Ma Cerro Galán Ignimbrite, NW Argentina, and comparison with other flow types. Bull Volcanol 73:1583–1609. https://doi.org/10.1007/s00445-011-0564-y

Chédeville C, Roche O (2018) Autofluidization of collapsing bed of fine particles: implications for the emplacement of pyroclastic flows. J Volcanol Geotherm Res 368:91–99. https://doi.org/10.1016/jvolgeores.2018.11.007

Dade WB, Huppert HE (1996) Emplacement of the Taupo ignimbrite by a dilute turbulent flow. Nature 381:509–512

Dartevelle S (2004) Numerical modeling of geophysical granular flows: 1. A comprehensive approach to granular rheologies and geophysical multiphase flows. Geochem Geophys Geosyst 5:Q08003. https://doi.org/10.1029/2003GC000636

Dartevelle S, Valentine GA (2007) Transient multiphase processes during the explosive eruption of basalt through a geothermal borehole (Námafjall, Iceland, 1977) and implications for natural volcanic flows. Earth Planet Sci Lett 262:363–384. https://doi.org/10.1016/j.epsl.2007.07.053

Dartevelle S, Valentine GA (2008) Multiphase magmatic flows at Yucca Mountain, Nevada. J Geophys Res 113:B12209. https://doi.org/10.1029/2007JB005367

Dartevelle S, Rose WI, Stix J, Kelfoun K, Vallance JW (2004) Numerical modeling of geophysical granular flows: 2. Computer simulations of plinian clouds and pyroclastic flows and surges. Geochem Geophys Geosyst 5:Q08004. https://doi.org/10.1029/2003GC000637

Dellino P, Zimanowski B, Büttner R, La Volpe L, Mele D, Sulpizio R (2007) Large-scale experiments on the mechanics of pyroclastic flows: design, engineering, and first results. J Geophys Res Sol Earth 112:B04202. https://doi.org/10.1029/2006JB004313

Dellino P, Dioguardi F, Mele D, D'Addabbo M, Zimanowski B, Büttner R, Doronzo DM, Sonder I, Sulpizio R, Dürig T, La Volpe L (2014) Volcanic jets, plumes, and collapsing fountains: evidence from large-scale experiments, with particular emphasis on the entrainment rate. Bull Volcanol 76:834–818. https://doi.org/10.1007/s00445-014-0834-6

Dellino P, Dioguardi F, Doronzo DM, Mele D (2019) The rate of sedimentation from turbulent suspension: an experimental model with application to pyroclastic density currents and discussion on the grain-size dependence of flow runout. Sedimentology 66:129–145. https://doi.org/10.1111/sed.12485

Dobran F, Neri A, Macedonio G (1993) Numerical simulation of collapsing volcanic columns. J Geophys Res Sol Earth 98:4231–4259

Doronzo DM, Valentine GA, Dellino P, de Tullio MD (2010) Numerical analysis of the effect of topography on deposition from dilute pyroclastic density currents. Earth Planet Sci Lett 300:164–173. https://doi.org/10.1016/epsl.2010.10.003

Doyle EE, Hogg AJ, Mader HM, Sparks RSJ (2008) Modeling dense pyroclastic flows from collapsing columns. Geophys Res Lett 35: L04305. https://doi.org/10.1029/2007GL032585

Druitt TH (1985) Vent evolution and lag breccia formation during the Cape Riva eruption of Santorini, Greece. J Geol 93:439–454

Druitt TH, Bacon CR (1986) Lithic breccia and ignimbrite erupted during the collapse of crater Lake caldera, Oregon. J Volcanol Geotherm Res 29:1–32

Druitt TH, Sparks RSJ (1982) A proximal ignimbrite breccia facies on Santorini, Greece. J Volcanol Geotherm Res 13:147–171

Druitt TH, Calder ES, Cole PD, Norton GE, Ritchie LJ, Sparks RSJ, Voight B (2002) Small-volume, highly mobile pyroclastic flows formed by rapid sedimentation from pyroclastic surges at Soufrière Hills Volcano, Montserrat: an important volcanic hazard. Geol Soc Lond Memoir 21:263–281

Dufek J (2015) The fluid mechanics of pyroclastic density currents. J Fluid Mech 48:459–485. https://doi.org/10.1146/annurev-fluid-122414-034252

Dufek J, Bergantz GW (2007a) Dynamics and deposits generated by the Kos Plateau Tuff eruption: controls of basal particle loss on pyroclastic flow transport. Geochem Geophys Geosys 8:Q12007. https://doi.org/10.1029/2007GC001741

Dufek J, Bergantz GW (2007b) Suspended load and bed-load transport of particle-laden gravity currents: the role of particle-bed interaction. Theor Comp Fluid Dyn 21:119–145. https://doi.org/10.1007/s00162-007-0041-6

Dufek J, Manga M (2008) In situ production of ash in pyroclastic flows. J Geophys Res Sol Earth 113:B09207. https://doi.org/10.1029/2007JB005555

Dufek J, Wexler J, Manga M (2009) Transport capacity of pyroclastic density currents: experiments and models of substrate-flow interaction. J Geophys Res Sol Earth 114:B11203. https://doi.org/10.1029/2008JB006216

Ergun S (1952) Fluid flow through packed columns. Chem Eng Prog 48:89–94

Esposti Ongaro T, Clarke AB, Neri A, Voight B, Widiwijayanti C (2008) Fluid dynamics of the 1997 Boxing Day volcanic blast at Monterrat, West Indies. J Geophys Res Sol Earth 113:B03211. https://doi.org/10.1029/2006JB004898

Esposti Ongaro T, Clarke AB, Neri A, Voight B, Widiwijayanti C (2012) Multiphase flow dynamics of pyroclastic density currents during the May 18, 1980 lateral blast of Mount St. Helens. J Geophys Res Sol Earth 117:B06208. https://doi.org/10.1029/2011JB009081

Esposti Ongaro T, Orsucci S, Cornolti F (2016) A fast, calibrated model for pyroclastic density currents kinematics and hazard. J Volcanol Geotherm Res 237:257–272. https://doi.org/10.1016/j.jvolgeores.2016.08.002

Fauria KE, Manga M, Chamberlain M (2016) Effect of particle entrainment on the runout of pyroclastic density currents. J Geophys Res Sol Earth 121. https://doi.org/10.1002/2016JB013263

Fierstein J, Wilson CJN (2005) Assembling an ignimbrite: compositionally defined eruptive packages in the 1912 Valley of Ten Thousand Smokes ignimbrite, Alaska. Geol Soc Am Bull 117:1094–1107. https://doi.org/10.1130/B25621.1

Fisher RV (1990) Transport and deposition of a pyroclastic surge across an area of high relief: the 18 May 1980 eruption of Mount St. Helens, Washington. Geol Soc Am Bull 102:1038–1054. https://doi.org/10.1130/0016-7606(1990)102<1038:TADOAP>2.3.CO;2

Gidaspow D (1994) Multiphase flow and fluidization: continuum and kinetic theory descriptions with applications. Academic Press, San Diego

Johnson PC, Jackson R (1987) Frictional-collisional constitutive relations for granular materials, with applications to plane shearing. J Fluid Mech 176:67–93

Kelfoun K (2017) A two-layer depth-averaged model for both the dilute and the concentrated parts of pyroclastic currents. J Geophys Res Sol Earth 122:4293–4311. https://doi.org/10.1002/2017JB014013

Kelfoun K, Samaniego P, Palacios P, Barba D (2009) Is frictional behaviour suitable for pyroclastic flow simulation: comparison with a well constrained eruption at Tungurahua volcano (Equador). Bull Volcanol 71:1057–1075. https://doi.org/10.1007/s00445-009-0286-6

Lube G, Cronin SJ, Platz T, Freundt A, Procter JN, Henederson C, Sheridan MF (2007) Flow and deposition of pyroclastic granular flows: a type example from the 1975 Ngauruhoe eruption, New Zealand. J Volcanol Geotherm Res 161:165–186. https://doi.org/10.1016/j.jvolgeores.2006.12.003

Lube G, Breard ECP, Cronin SJ, Jones J (2015) Synthesizing large-scale pyroclastic flows: experimental design, scaling, and first results from PELE. J Geophys Res Sol Earth 120:1487–1502. https://doi.org/10.1002/2014JB011666

Marble FE (1970) Dynamics of dusty gases. Ann Rev Fluid Mech 2:397–446

Moitra P, Sonder I, Valentine GA (2018) Effects of size and temperature-dependent thermal conductivity on the cooling of pyroclasts in air. Geochem Geophys Geosyst 19:3623–3636. https://doi.org/10.1029/2018GC007510

Neri A, Dobran F (1994) Influence of eruption parameters on the thermofluid dynamics of collapsing volcanic columns. J Geophys Res 99:11833–11857

Neri A, Ongaro TE, Macedonio G, Gidaspow D (2003) Multiparticle simulation of collapsing volcanic columns and pyroclastic flow. J Geophys Res Sol Earth 108:2202. https://doi.org/10.1029/2001JB000508

Neri A, Bevilacqua A, Esposti Ongaro T, Isaia R, Aspinall WP, Bisson M, Flandoli F, Baxter PJ, Bertagnini A, Iannuzzi E, Orsucci S, Pistolesi M, Rosi M, Vitale S (2015) Quantifying volcanic hazard at Campi Flegrei caldera (Italy) with uncertainty assessment: 2. Pyroclastic density current invasion maps. J Geophys Res Sol Earth 120:2330–2349. https://doi.org/10.1002/2014JB011776

Ort MH, Orsi G, Pappalardo L, Fisher RV (2003) Anisotropy of magnetic susceptibility studies of depositional processes in the Campanian ignimbrite, Italy. Bull Volcanol 65:55–72. https://doi.org/10.1007/s00445-002-0241-2

Patra AK, Bauer AC, Nichita CC, Pitman EB, Sheridan MF, Bursik M, Rupp B, Webber A, Stinton AJ, Namikawa LM, Renschler CS (2005) Parallel adaptive numerical simulation of dry avalanches over natural terrain. J Volcanol Geotherm Res 139:1–22

Perrotta A, Scarpati C (1994) The dynamics of the Brecca Museo eruption (Campi Flegrei, Italy) and the significance of spatter clasts associated with lithic breccias. J Volcanol Geotherm Res 59:335–355

Roche O (2012) Depositional processes and gas pore pressure in pyroclastic flows: an experimental perspective. Bull Volcanol 74:1807–1820. https://doi.org/10.1007/s00445-012-0639-4

Roche O, Carazzo G (2019) The contribution of experimental volcanology to the study of the physics of eruptive processes, and related scaling issues: a review. J Volcanol Geotherm Res 384:103–150. https://doi.org/10.1016/j.jvolgeores.2019.07.011

Roche O, Gilbertson MA, Phillips JC, Sparks RSJ (2005) Inviscid behaviour of fines-rich pyroclastic flows inferred from experiments on gas-particle mixtures. Earth Planet Sci Lett 240:401–414. https://doi.org/10.1016/j.epsl.2005.09.053

Roche O, Montserrat S, Niño Y, Tamburrino A (2008) Experimental observations of water-like behavior of initially fluidized, dam break granular flows and their relevance for the propagation of ash-rich pyroclastic flows. J Geophys Res Sol Earth 113:B12203. https://doi.org/10.1029/2008/JB005664

Roche O, Montserrat S, Niño Y, Tamburrino A (2010) Pore fluid pressure and internal kinematics of gravitational laboratory air-particle flows: insights into the emplacement dynamics of pyroclastic flows. J Geophys Res 115:B09206. https://doi.org/10.1029/2009JB007133

Roche O, Attali M, Mangeney A, Lucas A (2011) On the run-out distance of geophysical gravitational flows: insight from fluidized granular collapse experiments. Earth Planet Sci Lett 311:375–385. https://doi.org/10.1016/j.epsl.2011.09.023

Roche O, Niño Y, Mangeney A, Brand B, Pollock N, Valentine GA (2013) Dynamic pore pressure variations induce substrate erosion by pyroclastic flows. Geology 41:1107–1110. https://doi.org/10.1130/G34668.1

Roche O, Buesch DC, Valentine GA (2016) Slow-moving, far-travelled dense pyroclastic flows during the peach spring super-eruption. Nat Commun 7:10890. https://doi.org/10.1038/NCOMMS10890

Shimizu HA, Koyaguchi T, Suzuki YJ (2019) The run-out distance of large-scale pyroclastic density currents: a two-layer depth-averaged model. J Volcanol Geotherm Res 381:168–184. https://doi.org/10.1016/j.jvolgeores.2019.03.013

Srivastava A, Sundaresan S (2003) Analysis of a frictional-kinetic model for gas-particle flow. Powder Tech 129:72–85

Sulpizio R, Dellino P, Doronzo DM, Sarocchi D (2014) Pyroclastic density currents: state of the art and perspectives. J Volcanol Geotherm Res 283:36–65. https://doi.org/10.1016/j.volgeores.2014.06.014

Suzuki-Kamata K, Kamata H (1990) The proximal facies of the Tosu pyroclastic-flow deposit erupted from Aso caldera, Japan. Bull Volcanol 52:325–333

Sweeney MR, Valentine GA (2015) Transport and mixing dynamics from explosions in debris-filled volcanic conduits: numerical results and implications for maar-diatreme volcanoes. Earth Planet Sci Lett 425: 64–76. https://doi.org/10.1016/j.epsl.2015.05.038

Sweeney MR, Valentine GA (2017) Impact zone dynamics of dilute mono-and polydisperse jets and their implications for initial conditions of pyroclastic density currents. Phys Fluids 29:093304. https://doi.org/10.1063/1/5004197

Syamlal M (1987) The particle-particle drag term in a multiparticle model of fluidization. US Dept Energy Tech Rep DOE/MC/21353-2373

Syamlal M, Pannala S (2011) Multiphase continuum formulation for gassolids reacting flows. In: Pannala S, Syamlal M, O'Brien TJ (eds) Computational gas-solids flows and reacting systems: theory, Methods and Practice. IGI Global, Hershey, pp 1–65

Syamlal M, Musser J, Dietiker J-F (2017) Two-fluid model in MFIX. In: Michaelides EE, Crowe CT, Schwarzkopf JD (eds) Multiphase flow handbook, 2nd edn. CRC Press, Boca Raton, pp 242–275

Tierz P, Stefanescu ER, Sandri L, Sulpizio R, Valentine GA, Marzocchi W, Patra A (2018) Towards quantitative volcanic risk of pyroclastic density currents: probabilistic hazard curves and maps around Somma-Vesuvius (Italy). J Geophys Res Sol Earth 123:6299–6317. https://doi.org/10.1029/2017JB015383

Valentine GA, Sweeney MR (2018) Compressible flow phenomena at inception of lateral density currents fed by collapsing gas-particle mixtures. J Geophys Res Sol Earth 123:1286–1302. https://doi.org/10.1002/2017JB015129

Valentine GA, Wohletz KH (1989) Numerical models of Plinian eruption columns and pyroclastic flows. J Geophys Res 94:1867–1887

Valentine GA, Wohletz KH, Kieffer SW (1992) Effects of topography on facies and compositional zonation in caldera-related ignimbrites. Geol Soc Am Bull 104:154–165. https://doi.org/10.1130/0016-7606(1992)104<0154:EOTOFA>2.3.CO;2

Valentine GA, Palladino DM, DiemKaye K, Fletcher C (2019) Lithic-rich and lithic-poor ignimbrites and their basal deposits: Sovana and Sorano formations (Latera caldera, Italy). Bull Volcanol 81:29–26. https://doi.org/10.1007/s00445-019-1288-7

Walker GPL (1985) Origin of coarse lithic breccias near ignimbrite source vents. J Volcanol Geotherm Res 25:157–171

Weit A, Roche O, Dubois T, Manga M (2018) Experimental measurement of the solid particle concentration in geophysical turbulent gas-particle mixtures. J Geophys Res Sol Earth 123. https://doi.org/10.1029/2018JB015530

Weit A, Roche O, Dubois T, Manga M (2019) Maximum solid phase concentration in geophysical turbulent gas-particle flows: insights from laboratory experiments. Geophys Res Lett 46:6388–6396. https://doi.org/10.1029/2019GL082658

Wilson CJN (1985) The Taupo eruption, New Zealand II: the Taupo ignimbrite. Phil Trans R Soc London Ser A 314:229–310

Wilson CJN, Hildreth W (1997) The bishop tuff: new insights from eruptive stratigraphy. J Geol 105:407–439

Wright JV, Walker GPL (1977) Significance of a co-ignimbrite lag-fall deposit. Geology 5:729–732

Yasuda Y, Suzuki-Kamata K (2018) The origin of a coarse lithic breccia in the 34 ka caldera-forming Sounkyo eruption, Taisetsu volcano group, Central Hokkaido, Japan. J Volcanol Geotherm Res 357: 287–305. https://doi.org/10.1016/j.jvolgeores.2018.04.017